ISSN 2409-5613 (print)
ISSN 2411-1414 (online)

Chimica Techno Acta

2018. Vol. 5. N 4

cta.urfu.ru

Founded by Ural Federal University named after the first President of Russia B. N. Yeltsin
19, Mira St., Ekaterinburg, 620002, Russia

Учредитель — Уральский федеральный университет имени первого Президента России Б. Н. Ельцина
620002, Россия, Екатеринбург, ул. Мира, 19

Chimica Techno Acta

2018 | Vol. 5 | № 4

Scientific and Technical Journal
Established in 2014
Published four times per year

Chimica Techno Acta

Chimica Techno Acta

2018 | Vol. 5 | № 4

Научно-технический журнал
Журнал основан в 2014 г.
Выходит четыре раза в год

Chimica Techno Acta

Graphical Abstracts

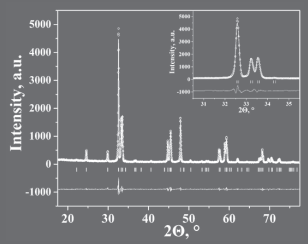

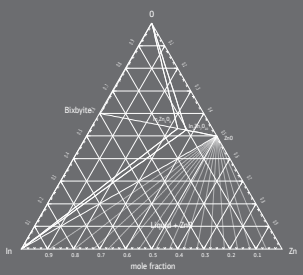

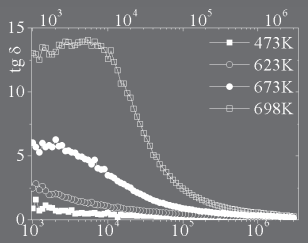

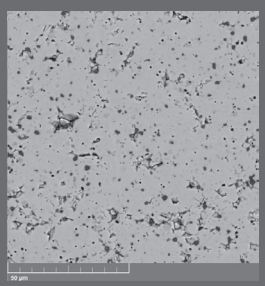

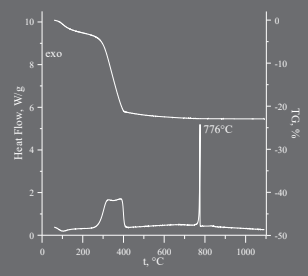

CONTENTS/СОДЕРЖАНИЕ

Chimica Techno Acta
2018. Vol. 5, № 4

This issue is dedicated to Professor Alexander Petrov, whose 75th birthday we have celebrated this year. During all his life Alexander Petrov was deeply involved into teaching and research in the Chemical Faculty of the Ural State University. His research interests included wide range of topics concerning thermodynamics and stability of oxide systems, crystal and defect structure, charge and mass transfer, technical applications of oxide materials, and many others. Professor Petrov is a co-author of many publications, patents, and text-books. Together with his teacher, Professor Vladimir Zhukovsky, Alexander Petrov became a founder of outstanding research group for Solid State Chemistry in the Ural State University, which raised many talented young scientists.

He was one of the first scientists of the Ural State University who managed to go on an internship abroad, to Professor P. Kofstad. As a result, since mid-70th, Oslo University remains our good partner for collaboration in different forms. Later, Professor Petrov took part in research in well-known research centers in Italy, Denmark, USA, and many others, and delivered lectures at international conferences as an invited speaker.

For 22 years (1986–2008) Professor Petrov headed the Department of Physical Chemistry in the Ural State University. During that time, he made a lot of effort to maintain close collaboration with Institutes of Ural Branch of the Russian Academy of Science and its predecessor — the Academy of Science of the USSR. In 1987, he organized a joint laboratory with the Institute of Electrophysics. A branch of the Department of Physical Chemistry was established in 1995 in the Institute of High-Temperature Electrochemistry. A scientific laboratory "Neutron-diffraction studies of complex oxides" was organized jointly with the Institute for Metal Physics in 1997. It can be said that Professor Petrov anticipated the trends that the Ministry of Science and Higher Education of Russia is currently implementing.

Alexander Petrov repeatedly won high awards. For example, in 1989 together with others he was awarded by the Prize of the Council of Ministers of the USSR for the development of novel ceramic cathodes for CO_2-lasers, in 2000 he was awarded the State Scholarship for Outstanding Scholars of the Russian Federation, in 2001 he was awarded the Honored Scientist of the Russian Federation title.

In addition to his merits and titles, the most important traits of Alexander Petrov were his outstanding humanity and decency. He was always ready to fight for justice and come to the rescue. More than 10 years have passed since he is not with us, but we still keep bright memories and warm feelings towards him in our hearts.

Galayda A. P., Volkova N. E., Dyagileva A. I.,
Gavrilova L. Ya., Cherepanov V. A., Battle P. D.
Chimica Techno Acta. 2018. Vol. 5, No. 4. P. 159–165.
ISSN 2409–5613

DOI: 10.15826/chimtech.2018.5.4.01

A. P. Galayda[a*], N. E. Volkova[a], A. I. Dyagileva[a], L. Ya. Gavrilova[a], V. A. Cherepanov[a], P. D. Battle[b]

[a] *Institute of Natural Sciences and Mathematics, Ural Federal University, 19 Mira St., Ekaterinburg, 620002, Russian Federation*
[b] *Inorganic Chemistry Laboratory, University of Oxford, South Parks Road, Oxford OX1 3QR, UK*
**E-mail: anastasia.galaida@urfu.ru*

Crystal structure and properties of novel oxide $Sm_{0.9}Ca_{1.1}Fe_{0.7}Co_{0.3}O_{4-\delta}$

$Sm_{0.9}Ca_{1.1}Fe_{0.7}Co_{0.3}O_{4-\delta}$ oxide with the K_2NiF_4-type structure was prepared using a glycerin-nitrate technique. The XRD pattern of $Sm_{0.9}Ca_{1.1}Fe_{0.7}Co_{0.3}O_{4-\delta}$ was refined by the Rietveld method within an orthorhombic structure (space group *Bmab*). The electrical conductivity, Seebeck coefficient, and thermal expansion of $Sm_{0.9}Ca_{1.1}Fe_{0.7}Co_{0.3}O_{4-\delta}$ were measured depending on temperature in air. The change of oxygen nonstoichiometry determined by TGA in air does not exceed 0.01. The oxygen content in $Sm_{0.9}Ca_{1.1}Fe_{0.7}Co_{0.3}O_{4-\delta}$ determined by the reduction in a hydrogen flux is equal to 3.96 ± 0.01. The positive value of Seebeck coefficient indicates that the predominant charge carriers in the oxide studied are electron holes.

Keywords: complex oxide; Ruddlesden-Popper phase; crystal structure; oxygen nonstoichiometry, electroconductivity; thermal expansion.

Received: 13.11.2018. Accepted: 05.12.2018. Published: 31.12.2018.

Introduction

Complex oxides with the K_2NiF_4-type structure based on rare earth, alkaline earth and 3d-transition metals are known as materials with high mixed electronic-ionic conductivity and oxygen mobility, and also thermodynamic stability at high temperature under an oxidizing atmosphere [1–4]. For this reason, K_2NiF_4-type oxides have attracted much attention as promising SOFC cathodes [1–3], oxygen-separation membranes [5] and catalysts [6]. The crystal structure of a K_2NiF_4-type oxide is built up by alternating the perovskite layer (ABO_3) and rock salt layer (AO) [7]. Depending on the nature of the metals in the A and B sublattices, the crystal structure of oxides with overall composition A_2BO_4 can be described using a tetragonal (sp. gr. *I4/mmm*) or orthorhombic (sp. gr. *Bmab*) unit cell [3–13]. Compared with Sr-substituted phases, very little is known about Ca-doped analogues with the K_2NiF_4-type structure. It has been reported previously that metastable lanthanum calcium ferrite $CaLaFeO_{4-\delta}$ decomposes at 1100 °C to lanthanum ferrite $LaFeO_{3-\delta}$ and calcium oxide CaO [14]. One can expect that variation of the Ln/Ca ratio and partial substitution of more electronegative Co for Fe ions

in the B-site position will stabilize the K_2NiF_4-type structure. The present study has focused on the structure and properties of the novel $Sm_{0.9}Ca_{1.1}Fe_{0.7}Co_{0.3}O_{4-\delta}$ oxide with the K_2NiF_4-type structure.

Experimental

The complex oxide was prepared using a glycerin nitrate technique. Samarium oxide Sm_2O_3 (99.99% purity), calcium carbonate $CaCO_3$ ("pure for analysis" grade), metallic cobalt Co, iron oxalate $FeC_2O_4 \cdot 2H_2O$ ("pure for analysis" grade), nitric acid ("special purity" grade) and glycerin were used as the starting materials. Metallic cobalt was obtained by reducing cobalt oxide Co_3O_4 ("special purity" grade) in the hydrogen flow at 400–600 °C for 6 h. The appropriate stoichiometric amounts of starting materials were dissolved in nitric acid, and then glycerin was added to the solution. The resulting gel was dried in a porcelain cup, decomposed to the dark powder, then placed in an alumina crucible and calcined in air at 700–1000 °C for 8–10 h. The final annealing was performed at 1100 °C in air for 120 h with intermediate grindings, followed by slow cooling to room temperature at a rate of ~100 °C/h. The phase composition of the annealed samples was determined by X-ray diffraction using a Shimadzu XRD-7000 (CuKα-radiation, angle range 2Θ = 20–90°, step 0.03°, 5 s/step) in air. The structural parameters were refined by the Rietveld profile method using the Fullprof-2008 package. Thermogravimetric analysis (TGA) was carried out using an STA 409 PC instrument (Netzsch) over the temperature range 25–1100 °C in air in dynamic (heating/cooling rate 2 K/min) mode. The absolute values of oxygen content were determined by a reduction of the samples in a hydrogen flux inside the TGA cell at 1200 °C [15]. Thermal expansion measurements were carried out within the temperature range of 25–1100 °C in air using a dilatometer DIL 402C (Netzsch) at a heating/cooling rate of 5K/min. The total conductivity and Seebeck coefficients of ceramic samples were measured in air by a 4-probe method with platinum electrodes. A bar-shaped sample (3×4×25 mm) for thermal expansion coefficient (TEC) and conductivity measurements was obtained by pressing powder that was mixed with 2–3 drops of ethanol using a manually-operated press. Afterwards, the samples prepared accordingly were slow heated and then sintered at 1200 °C for 14 h in air followed by slow cooling (the rate of heating and cooling was 50 K/h). The relative density of the sample was evaluated by a comparison of measured values to those calculated from the XRD-data. The relative density was found to be 90%.

Results and discussion

In contrast with previously reported $SmCaCoO_{4-\delta}$ [10] and $LnSrFeO_{4-\delta}$ (Ln=La [16], Nd [17, 18], Gd [19], Sm [13]), we have failed to synthesize samarium-calcium ferrite with an equimolar Sm/Ca-ratio at 1100 °C in air. It is known that the homogeneity range limits for such solid solutions depend significantly on temperature, ionic radius of dopants and oxygen partial pressure. The decrease of temperature from 1500 °C to 1100 °C leads to decomposition of $CaLaFeO_{4-\delta}$ to $LaFeO_{3-\delta}$ and CaO [14].

The complex oxide $Sm_{0.9}Ca_{1.1}Fe_{0.7}Co_{0.3}O_{4-\delta}$ was prepared

by a standard glycerin-nitrate technique with annealing temperature 1100 °C in air. Diffraction data for $Sm_{0.9}Ca_{1.1}Fe_{0.7}Co_{0.3}O_{4-\delta}$ analyzed by the Rietveld method are shown in Fig. 1. XRD pattern of $Sm_{0.9}Ca_{1.1}Fe_{0.7}Co_{0.3}O_{4-\delta}$ was indexed in the orthorhombic structure (sp. gr. *Bmab*).

The value of the oxygen content in $Sm_{0.9}Ca_{1.1}Fe_{0.7}Co_{0.3}O_{4-\delta}$ at room temperature determined by the TGA reduction was found to be 3.96 ± 0.01, and is consistent with that for $SmCaCoO_{4-\delta}$ [10]. The TGA measurements within the temperature range of 25–1100 °C in air revealed a small change in oxygen content, 4-δ, that is less than 0.01 (Fig. 2).

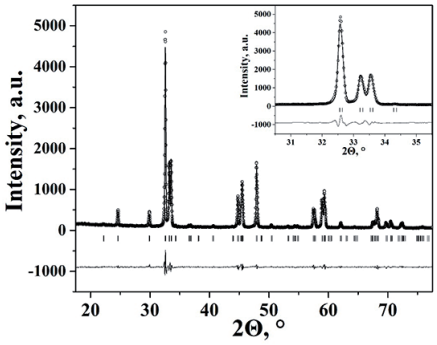

Fig. 1. Rietveld refined XRD pattern of $Sm_{0.9}Ca_{1.1}Fe_{0.7}Co_{0.3}O_{4-\delta}$. Circles are the experimental XRD data, upper continuous line is the calculated profile, lower continuous line is the difference plot, vertical lines are indicating the Bragg positions

The temperature dependence of the thermal expansion in air for $Sm_{0.9}Ca_{1.1}Fe_{0.7}Co_{0.3}O_{4-\delta}$ is given in Fig. 3 in comparison with $SmCaCoO_{4-\delta}$ [10].

As can be seen, the shape of the measured dependence is non-linear. Since this phenomenon cannot be explained by a noticeable oxygen exchange, we suggest that the non-linearity of the dilatometric plot is mainly associated with redistribution of electron density between Co and Fe and/or changes in Co spin states with the temperature. Similar behavior was observed in $SmFe_{1-x}Co_xO_{3-\delta}$ (x = 0.2, 0.5, 0.8) [10]. However, additional research is needed to clarify this behavior. The dependence of $\Delta L/L=f(T)$ has been described by two linear equations in the temperature ranges of 25–400 °C and 730–1000 °C. Low- and high-temperature TEC values for $Sm_{0.9}Ca_{1.1}Fe_{0.7}Co_{0.3}O_{4-\delta}$ in comparison with those of $SmCaCoO_{4-\delta}$ and most common SOFC electrolytes are listed in Table 1. The decrease in the TEC value with the increase of iron content can be explained by the higher bond energy

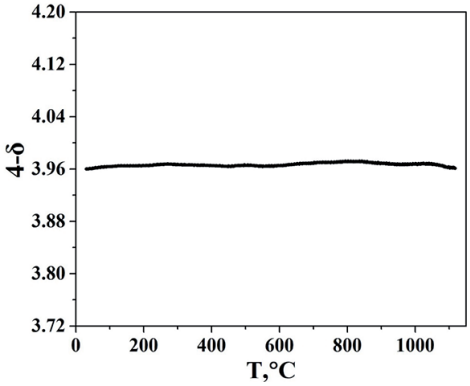

Fig. 2. Oxygen content, 4–δ, in $Sm_{0.9}Ca_{1.1}Fe_{0.7}Co_{0.3}O_{4-\delta}$ as a function of temperature in air

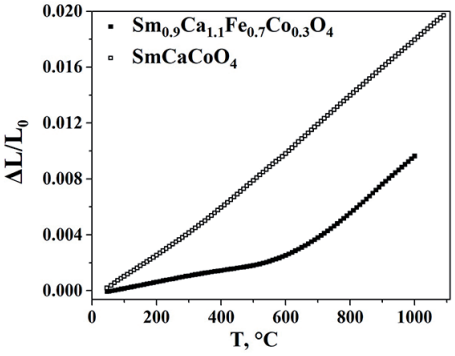

Fig. 3. Thermal expansion of the $Sm_{0.9}Ca_{1.1}Fe_{0.7}Co_{0.3}O_{4-\delta}$ and $SmCaCoO_{4-\delta}$ [10] ceramics in air

Table 1

The average thermal expansion coefficients for $Sm_{0.9}Ca_{1.1}Fe_{0.7}Co_{0.3}O_{4-\delta}$, $SmCaCoO_{4-\delta}$ [10] and SOFC electrolytes $Zr_{0.85}Y_{0.15}O_{2-\delta}$ [22] and $Ce_{0.8}Sm_{0.2}O_{2-\delta}$ [23] in air

Composition	Temperature range, °C	TEC×10^6, K^{-1}
$Sm_{0.9}Ca_{1.1}Fe_{0.7}Co_{0.3}O_{4-\delta}$	25–400	4.4
	730–1000	20.2
$SmCaCoO_{4-\delta}$ [10]	25–580	17.7
	580–1100	20.2
$Zr_{0.85}Y_{0.15}O_{2-\delta}$ [22]	30–1000	10.9
$Ce_{0.8}Sm_{0.2}O_{2-\delta}$ [23]	30–1000	12.5

for Fe–O (409 kJ/mol) compared to Co–O (368 kJ/mol) [20].

The total conductivity of $Sm_{0.9}Ca_{1.1}Fe_{0.7}Co_{0.3}O_{4-\delta}$ versus temperature is shown in Fig. 4.

The conductivity of $Sm_{0.9}Ca_{1.1}Fe_{0.7}Co_{0.3}O_{4-\delta}$ monotonously increases with temperature up to 23 S/cm at 1100 °C. In contrast, the Seebeck coefficient decreases with temperature. The positive value of the Seebeck coefficient (see Fig. 5) indicates that electron holes are the predominant charge carriers in the oxide studied. The conductivity activation energies calculated from two linear segments of Arrhenius plot (see insert in Fig. 4) are equal to 0.193 eV and 0.283 eV in the temperature ranges 50–250 °C and 300–1100 °C, respectively. Both values are typical for a hopping conduction mechanism.

A comparison of the temperature dependences of the total conductivity of $Sm_{0.9}Ca_{1.1}Fe_{0.7}Co_{0.3}O_{4-\delta}$ and $SmCaCoO_{4-\delta}$ [10] (see Fig. 4) visually shows that they coincide in practical term up to 600 °C and the conductivityhas thermally activated character for both oxides. A strong increase in the conductivity of $SmCaCoO_{4-\delta}$ above 600 °C can be explained by the pronounced charge disproportionation process at higher temperatures:

$$2Co_{Co}^{\times} \leftrightarrow Co_{Co}^{\circ} + Co_{Co}' \qquad (1)$$

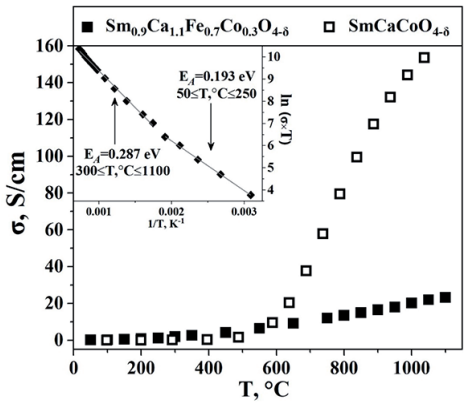

Fig. 4. Total conductivity of $Sm_{0.9}Ca_{1.1}Fe_{0.7}Co_{0.3}O_{4-\delta}$ and $SmCaCoO_{4-\delta}$ [10] versus temperature in air. The insert shows the Arrhenius plot for $Sm_{0.9}Ca_{1.1}Fe_{0.7}Co_{0.3}O_{4-\delta}$

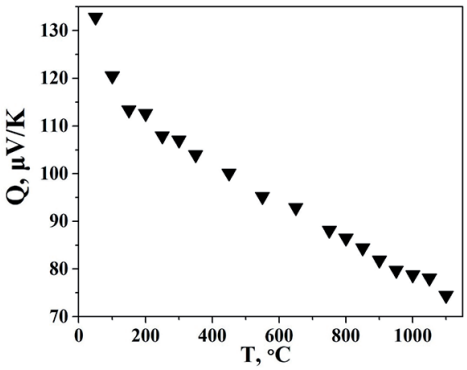

Fig. 5. Seebeck coefficient for $Sm_{0.9}Ca_{1.1}Fe_{0.7}Co_{0.3}O_{4-\delta}$ vs. temperature in air

In contrast, simultaneous presence of Co and Fe at the B-sites suppress disproportionation of iron and cobalt by the following process:

$$Fe^{\times}_{Fe} + Co^{\times}_{Fe} \leftrightarrow Fe^{\circ}_{Fe} + Co'_{Fe}, \quad (2)$$

where iron seems to be a hole trap [21].

Conclusions

Single-phase $Sm_{0.9}Ca_{1.1}Fe_{0.7}Co_{0.3}O_{4-\delta}$ was successfully synthesized by a glycerin nitrate technique. The structural parameters of the oxide prepared were refined by the Rietveld method. The oxygen content, 4–δ, at room temperature was found to be 3.96 ± 0.01 and its decrease with temperature does not exceeded 0.01. The lower value of the total conductivity of $Sm_{0.9}Ca_{1.1}Fe_{0.7}Co_{0.3}O_{4-\delta}$ compared to that of $SmCaCoO_{4-\delta}$ was explained in terms of an electronic exchange process. The Seebeck coefficient of $Sm_{0.9}Ca_{1.1}Fe_{0.7}Co_{0.3}O_{4-\delta}$ was shown to be positive over the entire temperature range investigated, indicating predominantly p-type conductivity.

Acknowledgements

This work was supported in parts by Act 211 Government of the Russian Federation, agreement 02.A03.21.0006.

References

1. Istomin SYa, Antipov EV. Cathode materials based on perovskite-like transition metal oxides for intermediate temperature solid oxide fuel cells. *Russ Chem Rev.* 2013;82(7):686–700. DOI: 10.1070/RC2013v082n07ABEH004390.
2. Dailly J, Fourcade S, Largeteau A, Mauvy F, Grenier JC, Marrony M. Perovskite and A_2MO_4-type oxides as new cathode materials for protonic solid oxide fuel cells. *Electrochim Acta.* 2010;55(20):5847–53. DOI: 10.1016/j.electacta.2010.05.034.
3. Zhao F, Wang X, Wang Z, Peng R, Xia C. K_2NiF_4 type $La_{2-x}Sr_xCo_{0.8}Ni_{0.2}O_{4+\delta}$ as the cathodes for solid oxide fuel cells. *Solid State Ionics.* 2008;179:1450–3. DOI: 10.1016/j.ssi.2008.06.019.
4. Daroukh MAl, Vashook VV, Ullmann H, Tietz F, Arual Raj I. Oxides of the AMO_3 and A_2MO_4-type: structural stability, electrical conductivity and thermal expansion. *Solid State Ionics.* 2003;158:141–50. DOI: 10.1016/S0167-2738(02)00773–7.
5. Vashook VV, Yushkevich II, Kokhanovsky LV, Makhnach LV, Tolochko SP, Kononyuk IF, Ullmann H, Altenburg H. Composition and conductivity of some nickelates. *Solid State Ionics.* 1999;119:23–30. DOI: 10.1016/S0167-2738(98)00478–0.
6. Ling Z, Xuezhong W, Cunzhen L. Catalytic combustion of diesel soot over K_2NiF_4-type oxides $La_{2-x}K_xCuO_4$. *J Rare Earths.* 2008.;26(2):254–7. DOI: 10.1016/S1002-0721(08)60076–9.
7. Skinner SJ. Characterisation of $La_2NiO_{4+\delta}$ using in-situ high temperature neutron powder diffraction. *Solid State Sci.* 2003;5:419–26. DOI: 10.1016/S1293-2558(03)00050–5
8. Taguchi H, Nakade K, Hirota K. Synthesis and characterization of K_2NiF_4-type $CaLnCoO_4$ (Ln = Sm and Gd). *Mater Res Bull.* 2007;42:649–56. DOI: 10.1016/j.materresbull.2006.08.004.

9. Taguchi H, Kido H, Tabata T. Relationship between crystal structure and electrical property of K_2NiF_4-type $(Ca_{1-x}Nd_{1+x})CoO_{4-d}$. *Physica B.* 2004;344:271–7. DOI: 10.1016/j.physb.2003.09.270.
10. Galayda AP, Volkova NE, Gavrilova LYa, Balymov KG, Cherepanov VA. Phase equilibria, structure and properties of intermediate phases in the Sm_2O_3-Fe_2O_3-CoO and Sm_2O_3-CaO-CoO systems. *J Alloys Compd.* 2017;718:288–97. DOI: 10.1016/j.jallcom.2017.05.044.
11. Romero de Paz J, Fernández-Díaz MT, Hernández Velasco J, Sáez Puche R, Martinez JL. Crystal and Magnetic Structure of $PrCaCrO_4$. *J Solid State Chem.* 1999;142(1):29–32. DOI: 10.1006/jssc.1998.7973.
12. Thorogood GJ, Orain P-Y, Ouvry M, Piriou B, Tedesco T, Wallwork KS, Herrmann J, James M. Structure, crystal chemistry and magnetism of rare earth calcium-doped cobaltates: $Ln_{2-x}Ca_xCoO_{4+\delta}$ (Ln=Pr, Nd, Sm, Eu, Gd). *Solid State Sci.* 2011;13:2113–23. DOI: 10.1016/j.solidstatesciences.2011.08.008.
13. Volkova NE, Maklakova AV, Gavrilova LYa, Cherepanov VA. Phase equilibria, crystal structure, and properties of intermediate oxides in the Sm_2O_3–SrO–CoO system. *Eur J Inorg Chem.* 2017:3285–92. DOI: 10.1002/ejic.201700321.
14. Nguyen-Trut-Dinh MM, Vlasse M, Perrin M, Le Flem G. Un oxide magnetique bidimensionnel: $CaLaFeO_4$. *J Solid State Chem.* 1980;32:1–8. DOI: 10.1016/0022–4596(80)90262–5.
15. Volkova NE, Gavrilova LYa, Cherepanov VA, Aksenova TV, Kolotygin VA, Kharton VV. Synthesis, crystal structure and properties of $SmBaCo_{2-x}Fe_xO_{5+\delta}$. *J Solid State Chem.* 2013:204;219–23. DOI: 10.1016/j.jssc.2013.06.001.
16. Jennings AJ, Skinner SJ, Helgason Ö. Structural properties of $La_xSr_{2-x}FeO_{4\pm d}$ at high temperature and under reducing conditions. *J Solid State Chem.* 2003;175:207–17. DOI: 10.1016/S0022-4596(03)00248–2.
17. Ki-Woog S, Ki-Tae L. Characterization of $NdSrCo_{1-x}Fe_xO_{4+d}$ ($0 \le x \le 1.0$) intergrowth oxide cathode materials for intermediate temperature solid oxide fuel cells. *Ceram Int.* 2011;37:573–7. DOI: 10.1016/j.ceramint.2010.10.004.
18. Aksenova TV, Vakhromeeva AE, Elkalashy ShI, Urusova AS, Cherepanov VA. Phase equilibria, crystal structure, oxygen nonstoichiometry and thermal expansion of complex oxides in the Nd_2O_3–SrO–Fe_2O_3 system. *J Solid State Chem.* 2017;251:70–8. DOI: 10.1016/j.jssc.2017.04.015.
19. Singh S, Singh D. Effect of increasing Sr content on structural and physical properties of K_2NiF_4-type phase $GdSrFeO_4$. *Ceram Int.* 2017;43:3369–76. DOI: 10.1016/j.ceramint.2016.11.182.
20. Cottrell TL. The Strengths of Chemical Bonds. 2nd ed. London: Butterworth; 1958. 317 p.
21. Tai L-W, Nasrallah MM, Anderson HU, Sparlin DM, Sehlin SR. Structure and electrical properties of $La_{1-x}Sr_xCo_{1-y}Fe_yO_3$. Part 1. The system $La_{0.8}Sr_{0.2}Co_{1-y}Fe_yO_3$. *Solid State Ionics.* 1995;76:259–71. DOI: 10.1016/0167–2738(94)00244-m.
22. Tsipis EV, Kharton VV. Electrode materials and mechanisms in solid oxide fuel cells: brief review. *J Solid State Electrochem.* 2008;12(11):1367–91. DOI: 10.1007/s10008-008-0611-6.

23. Pikalova EYu, Murashkina AA, Maragou VI, Demin AK, Strekalovsky VN, Tsiakaras PE. CeO_2 based materials doped with lanthanides for applications in intermediate temperature electrochemical devices. *Int J Hydrogen Energy.* 2011;36:6175–83. DOI: 10.1016/j.ijhydene.2011.01.132.

Jantzen T., Hack K., Yazhenskikh E., Müller M.
Chimica Techno Acta. 2018. Vol. 5, No. 4. P. 166–188.
ISSN 2409–5613

DOI: 10.15826/chimtech.2018.5.4.02

T. Jantzen[a], K. Hack[a], E. Yazhenskikh[b], M. Müller[b]

[a] *GTT-Technologies, Kaiserstraße 103, D-52134 Herzogenrath, Germany*
[b] *Forschungszentrum Jülich GmbH, IEK-2, D-52425 Jülich, Germany*
E-mail: tj@gtt-technlogies.de

Thermodynamic assessment of oxide system In_2O_3-SnO_2-ZnO

The In_2O_3-SnO_2-ZnO system is of special interest for applications as transparent conducting oxides and also transparent semiconductors. In the present work, a thermodynamic assessment for this system is discussed using all available experimental data on phase equilibria and thermodynamic properties. All subsystems including elemental combinations were considered in order to generate a self-consistent Gibbs energy dataset for further calculation and prediction of thermodynamic properties of the system. The modified associate species model was used for the description of the liquid phase. Particular attention was given to two significant solid solution phases: Spinel with the formula $Zn_{(2-x)}Sn_{(1-x)}In_{2x}O_4$ based on Zn_2SnO_4 and Bixbyite based on In_2O_3 and extending strongly toward the $SnZnO_3$ composition according to the formula $In_{(2-2x)}Sn_xZn_xO_3$. In addition to the component oxides, nine quasi-binary compounds located in the In_2O_3-ZnO binary subsystem have also been included in the database as stoichiometric phases.

Keywords: phase diagram; thermodynamic modeling; indium oxide; bixbyite; spinel

Received: 28.11.2018. Accepted: 14.12.2018. Published: 31.12.2018.

Introduction

Compositions in the In_2O_3–SnO_2–ZnO ternary oxide system are of interest owing to their optical transparency combined with high electrical conductivity [1, 2]. Transparent conducting oxides (TCOs) can be used as electrodes in solar cells, flat panel displays and other commercial devices. Although TCOs are applied usually in film form, the study of bulk phase relations and physical properties can be useful for understanding fundamental materials properties. At the present time, ITO (tin-doped indium oxide) is the material of choice for TCO layers (e.g. in review [3]), but the increasing cost of indium metal and the development of new technologies will require alternative TCOs. According to Palmer [4] both SnO_2 and ZnO are good TCOs with conductivities comparable to ITO. Compositions from the In_2O_3–ZnO system with high Zn concentration are attractive due to their high electrical conductivity, optical transparency and excellent chemical stability [5, 6].

The materials from the system ZITO (Zn-In-Sn-O) [2] are promising replacements for ITO as TCO layers in many opto-electronic applications. ZITO contains less indium than ITO, which lowers the cost, and it has a broad window of compositions that allow the TCO layer to be adjusted (conductivity, etc.) for each

application. The bulk equilibrium phases of ZITO have been defined and exhibit two transparent and conductive regions: the bixbyite solid solution $In_{2-2x}Zn_xSn_xO_3$ and the homologous series of compounds $In_2Zn_kO_{k+3}$.

Thermodynamic modelling on the basis of reliable experimental data and appropriate Gibbs energy models for solid and liquid phases is a powerful tool for calculation and prediction of the thermodynamic properties and phase equilibria for various systems. Furthermore, such data can be applied for heat balance calculations, i.e. for information on the energetics of possible production processes. The quality and completeness of the thermodynamic databases used is a key prerequisite for reliable calculations. According to CALPHAD-type modelling all available experimental data (phase equilibria, mixing properties, component activities, etc.) are critically analyzed in terms of their consistency. Each phase in the system is treated by an appropriate Gibbs energy model with adjustable parameters (Gibbs energy of constituents, interaction parameters, etc.), which are optimized in accordance with the experimental information in order to generate a self-consistent dataset of Gibbs energies of all phases in a system.

In the present study the thermodynamic assessment of the oxide system In_2O_3–SnO_2–ZnO is presented using all available experimental data on phase equilibria and thermodynamic properties. The calculation of phase equilibria and the prediction of thermodynamic properties using the database for the In_2O_3-SnO_2-ZnO system can be helpful for developing and manufacturing TCOs for optoelectronic devices. The experimental information on the available thermodynamic properties (phase diagram, phase transition etc.) is used for the generation of self-consistent Gibbs energy datasets for all known phases and compounds in this ternary system.

The Gibbs energy of the liquid phase has been modelled using a non-ideal associate solution model proposed by Besmann and Spear [7]. This model has been successfully applied for the description of melts containing oxides and sulphides in our previous studies, e.g. in [8–10]. Solubilities in the solid state have been treated using the multi-sublattice approach which allows the description of experimentally determined solubilities. In the present study there are two solid solution series with different structure. The spinel phase with formula $(\underline{Zn}^{+2},In^{+3})_2(\underline{Sn}^{+4}, Zn^{+2})_1(O^{-2})_4$ includes Zn_2SnO_4, In_2SnO_4, Zn_2ZnO_4, In_2ZnO_4 as end-members. The model for bixbyite in form of $In_{(2-2x)}Sn_xZn_xO_3$ using the formula $(\underline{In}, Zn, Va)_1(\underline{In}, Sn)_1(O)_3$ allows description of the limited solubility from pure indium oxide extending to SnZn compounds.

The present database contains a gas phase, a multi-component liquid phase, 7 solid solutions and 27 solid stoichiometric compounds.

Thermodynamic models

The Gibbs energies of the elements were taken from the SGTE unary database [11] while the pure component oxides were taken from the SGTE Pure Substance database [12], the thermodynamic descriptions of the metallic systems were taken from the SGTE Solution database [13]. The thermodynamic data sources used in the present work are collected in Table 1.

The thermodynamic descriptions of the assessed stoichiometric compounds are presented in Table 2.

Table 1

Thermodynamic data sources used in present work

System	Source	System	Source
In-Sn	[13]	In_2O_3–SnO_2	This work
In-Zn	[13]	In_2O_3–ZnO	This work
Sn-Zn	[13]	SnO_2–ZnO	This work
In-O	This work	In_2O_3–SnO_2–ZnO	This work
Sn-O	This work	–	–
Zn-O	This work	–	–

The solid solution phases in the In_2O_3-SnO_2-ZnO system considered in the present work are given in Table 3 and are described below in more detail.

The molten oxide phase

The Gibbs energy of the liquid phase in the system is represented by the modified non-ideal associate species model [7]. The basic species In_2O_3, SnO_2 and ZnO along with one (quasi)binary species (Sn-Zn_2O_4) have been introduced as liquid components. Although the corresponding metallic species were added for the systems Me-O, the present work will attend to the melt oxide species only; the interactions between these oxides and other oxide species are responsible for the thermodynamic properties of the liquid phase. To provide equal weighting of each associate species with regard to its entropic contribution in the ideal mixing term, each species contains a total of two cations in its formula based on [7]. In addition, interactions between associate species were introduced in order to fine tune the thermodynamic description.

The molar Gibbs energy of the solution is presented by a three-term expression with contributions of the reference part, the ideal and the excess part taking into account binary interactions as follows:

$$G_m = \sum x_i {}^\circ G_i + RT \sum x_i \ln x_i + \\ + \sum \sum_{i<j} x_i x_j \sum_{v=0} L_{ij}^{(v)} \left(x_i - x_j \right)^v \qquad (1)$$

where x_i is the mole fraction of phase constituent i (including the associate species), ${}^\circ G_i$ is the molar Gibbs energy of the pure phase constituent i and is an interaction coefficient between components i and j, according to the Redlich — Kister polynomial. The $L_{ij}^{(v)}$ with v = 0, 1, 2 and ${}^\circ G_i$ are temperature dependent in the same way according to:

$$ {}^\circ G_i, L_{ij}^{(v)} = A + B \cdot T + c \cdot T \cdot \ln\left(T\right) + \\ + D \cdot T^2 + E \cdot T^{-1} + F \cdot T^3 \qquad (2)$$

Thermodynamic data for the liquid components are summarized in Table 3. The elemental systems In–O and Zn–O contain one stable oxide, In_2O_3 and ZnO, respectively, while in the system Sn-O two oxides were considered, Sn_2O_2 and Sn_2O_4. The liquid phase of the quasi-binary oxide systems will contain the basic oxides along with one (quasi)binary species ($SnZn_2O_4 \cdot 3/2$). No ternary species were necessary. The Gibbs energy of the binary species are taken from the SGTE Pure Substance database [12] without modifications. The G function of the liquid species $SnZn_2O_4 \cdot 3/2$ was derived using the melting data of the

Table 2

Thermodynamic properties of stoichiometric compounds assessed in this work

Compound	$\Delta_f H^{298}$, J/mol	S^0_{298}, J/mol · K	T (K)	C_p, J/mol·K
SnO	–289853	48.95	298–1250	$43.7399+0.01356023\cdot T+10\cdot T^{-2}-1.06\cdot 10^{-10}\cdot T^2$ [13]
Sn_3O_4	–1155713	151.23	298–1250	$163.5208+0.03448263\cdot T-2223847\cdot T^{-2}+5.57\cdot 10^{-10}\cdot T^2$
$SnIn_2O_5$	–1439306.47	187.51	298–1903	$197.5511+0.01742532\cdot T-4485329\cdot T^{-2}+3.968488\cdot 10^{-10}\cdot T^2$
			1903–2186	$213.5101+0.01006315\cdot T-2261462\cdot T^{-2}-3.721512\cdot 10^{-10}\cdot T^2$
$Sn_3In_4O_{12}$	–3458277.2	426.23	298–1903	$471.1432+0.04221281\cdot T-11194525\cdot T^{-2}+3.968488\cdot 10^{-10}\cdot T^2$
			1903–2186	$213.5101+0.01006315\cdot T-2261462\cdot T^{-2}+1.5626976\cdot 10^{-9}\cdot T^2$
$Zn_3In_2O_6$	–1975291.24	231.8	298–2186	$264.2621+0.02177245\cdot T-4512542\cdot T^{-2}+3.8375878488\cdot 10^{-6}\cdot T^2$
$Zn_4In_2O_7$	–2326518.2	274.79	298–2186	$311.8461+0.02567555\cdot T-4512542\cdot T^{-2}+3.8375878488\cdot 10^{-6}\cdot T^2$
$Zn_5In_2O_8$	–2678001	317.6	298–2186	$359.4301+0.02957865\cdot T-6013262\cdot T^{-2}+6.3962278488\cdot 10^{-6}\cdot T^2$
$Zn_6In_2O_9$	–3028592	360.86	298–2186	$407.0141+0.03348175\cdot T-6763622\cdot T^{-2}+7.6755478488\cdot 10^{-6}\cdot T^2$
$Zn_7In_2O_{10}$	–3379500	403.92	298–2186	$454.5981+0.03738485\cdot T-7513982\cdot T^{-2}+8.9548678488\cdot 10^{-6}\cdot T^2$
$Zn_9In_2O_{12}$	–4080212	490.44	298–2186	$549.7661+0.04519105\cdot T-9014702\cdot T^{-2}+1.15135078488\cdot 10^{-5}\cdot T^2$
$Zn_{11}In_2O_{14}$	–4781168.4	576.79	298–2186	$644.9341+0.05299725\cdot T-10515422\cdot T^{-2}+1.40721478488\cdot 10^{-5}\cdot T^2$
$Zn_{13}In_2O_{16}$	–5482137.2	663.13	298–2186	$644.9341+0.05299725\cdot T-10515422\cdot T^{-2}+1.40721478488\cdot 10^{-5}\cdot T^2$
$Zn_{15}In_2O_{18}$	–6183104.984	749.4702	298–2186	$835.2701+0.06860965\cdot T-13516862\cdot T^{-2}+1.91894278488\cdot 10^{-5}\cdot T^2$
$SnZn_2O_4$	–1282630	151	298–1903	$171.209+0.01516837\cdot T-3724587\cdot T^{-2}+2.55940900002\cdot 10^{-6}\cdot T^2$
			1903–2250	$187.168+0.0078062\cdot T-1500720\cdot T^{-2}+2.55864\cdot 10^{-6}\cdot T^2$

corresponding constituent oxides. The interactions between liquid species are listed in Table 3.

Spinel

Normal Spinels can be described using the formula AB_2O_4, where A is a divalent metallic cation and B represents a trivalent cation placed on the second sublattice. For example, zinc aluminate ($ZnAl_2O_4$) and zinc ferrite ($ZnFe_2O_4$) are normal spinels. On the other hand, zinc stannate Zn_2SnO_4 is an inverse spinel and has the chemical formula A_2BO_4 where A are divalent zinc cations and B tetravalent tin cations, as in $(Zn^{2+})_2(Sn^{4+})(O^{2-})_4$. The inverse Spinel Zn_2SnO_4 has the cubic spinel structure (space group) and Pearson symbol *cF56* [14]. This inverse spinel structure is present in many systems, e.g. as Ülvöspinel Fe_2TiO_4, manganese titanate Mn_2TiO_4 and gandilite Mg_2TiO_4. All of them can be treated with the same common formula

Table 3

Thermodynamic descriptions of the liquid and solid solution phases

Parameter value, J/mol	Reference
Liquid: (In, In_2O_3, Sn, Sn_2O_2, Sn_2O_4, Zn, Zn_2O_2, $SnZn_2O_4$/1.5)	*
$^{\circ}G_{In} = {}^{\circ}G^{SGPS}_{Liq-In}$	[11]
	[12]
$^{\circ}G_{In_2O_3} = {}^{\circ}G^{SGPS}_{Liq-Ti_2O_3}$	[11]
	[12]
$^{\circ}G_{Sn} = {}^{\circ}G^{SGPS}_{Liq-Sn}$	[12]
$^{\circ}G_{Sn_2O_2} = 2{}^{\circ}G^{SGPS}_{Liq-SnO}$	[11]
$^{\circ}G_{Sn_2O_4} = 2{}^{\circ}G^{SGPS}_{Liq-SnO_2}$	*
$^{\circ}G_{Zn} = {}^{\circ}G^{SGPS}_{Liq-Zn}$	*
$^{\circ}G_{SnZn_2O_4} = {}^{\circ}G^{Spinel}_{SnZn_2O_4} + 163400 - 80.81806 \bullet T$	*
$^{\circ}L^{liq}_{In,\,In_2O_3} = +27600$	*
$^{\circ}L^{liq}_{Sn,\,SnO} = +39000$	*
$^{1}L^{liq}_{Sn,SnO} = +11200$	*
$^{\circ}L^{liq}_{Sn,\,SnO_2} = +44000$	*
$^{\circ}L^{liq}_{In_2O_3,\,SnO_2} = -11000$	*
$^{\circ}L^{liq}_{In_2O_3,\,ZnO} = -11000$	*
$^{\circ}L^{liq}_{In_2O_3,SnO_2,Sn} = -187000$	*
Spinel: $(Zn^{2+}, \underline{Sn}^{4+})_1(\underline{Zn}^{2+}, In^{3+})_2(O^{2-})_4$	*
$^{\circ}G_{Zn^{2+}:Zn^{2+}:O^{2-}} = 0.5 \cdot {}^{\circ}G^{Spinel}_{SnZn_2O_4} + 0.5 \cdot {}^{\circ}G^{Spinel}_{ZnIn_2O_4} + 9500$	*
$^{\circ}G_{Zn^{2+}:In^{3+}:O^{2-}} = {}^{\circ}G^{Spinel}_{ZnIn_2O_4} = {}^{\circ}G^{SGPS}_{ZnO} + {}^{\circ}G^{SGPS}_{In_2O_3} + 27000$	*
$^{\circ}G_{Sn^{4+}:Zn^{2+}O^{2-}} = {}^{\circ}G^{Spinel}_{SnZn_2O_4}$	*
$^{\circ}G_{Sn^{4+}:In^{3+}:O^{2-}} = 0.5 \cdot {}^{\circ}G^{Spinel}_{SnZn_2O_4} + 0.5 \cdot {}^{\circ}G^{Spinel}_{ZnIn_2O_4} + 9500$	

Continuation of table 3

Parameter value, J/mol	Reference
Bixbyite: (<u>In</u>, Zn, Va)(<u>In</u>, Sn)$(O)_3$	*
$^{\circ}G_{\mathrm{In:In:O}} = {}^{\circ}G^{\mathrm{SGPS}}_{\mathrm{In_2O_3}}$	[12]
$^{\circ}G_{\mathrm{In:Sn:O}} = 0.5\cdot{}^{\circ}G^{\mathrm{SGPS}}_{\mathrm{In_2O_3}} + 0.5\cdot{}^{\circ}G^{\mathrm{Bixbyite}}_{\mathrm{ZnSnO_3}} + 20000 + 11\cdot T$	*
$^{\circ}G_{\mathrm{Zn:In:O}} = 0.5\cdot{}^{\circ}G^{\mathrm{SGPS}}_{\mathrm{In_2O_3}} + 0.5\cdot{}^{\circ}G^{\mathrm{Bixbyite}}_{\mathrm{ZnSnO_3}} + 119044 - 3\cdot T$	*
$^{\circ}G_{\mathrm{Zn:Sn:O}} = {}^{\circ}G^{\mathrm{Bixbyite}}_{\mathrm{ZnSnO_3}} = {}^{\circ}G^{\mathrm{SGPS}}_{\mathrm{ZnO}} + {}^{\circ}G^{\mathrm{SGPS}}_{\mathrm{SnO_2}} - 10800$	*
$^{\circ}G_{\mathrm{Va:In:O}} = 0.5\cdot{}^{\circ}G^{\mathrm{SGPS}}_{\mathrm{In_2O_3}}$	*
$^{\circ}G_{\mathrm{Va:Sn:O}} = {}^{\circ}G^{\mathrm{SGPS}}_{\mathrm{SnO_2}} + 12000$	*
$^{0}L^{\mathrm{Bixbyite}}_{\mathrm{In:In,Sn:O}} = -46403 + 13\bullet T$	
$^{0}L^{\mathrm{Bixbyite}}_{\mathrm{In,Zn:In:O}} = -10.52\bullet T$	
$^{0}L^{\mathrm{Bixbyite}}_{\mathrm{In,Zn:Sn:O}} = +1700$	
$^{0}L^{\mathrm{Bixbyite}}_{\mathrm{In,Zn:In,Sn:O}} = -318000$	
$^{1}L^{\mathrm{Bixbyite}}_{\mathrm{In,Zn:In,Sn:O}} = -97000$	

* — This work.

$(A^{2+})_2(B^{4+})(O^{2-})_4$. In the In_2O_3–SnO_2–ZnO ternary system the spinel phase Zn_2SnO_4 dissolves a significant amount of indium and extends toward the fictive $ZnO{\cdot}In_2O_3$ composition, having constant Zn:Sn ratio [1] according to the formula $Zn_{(2-x)}Sn_{(1-x)}In_{2x}O_4$. The proposed multi sublattice formula reads $(\underline{Zn}^{2+}, In^{3+})_2(\underline{Sn}^{4+}, Zn^{2+})_1(O^{2-})_4$ and allows to describe the deviation from the stoichiometric composition towards higher In_2O_3-contents keeping the Zn:Sn ratio to 2:1.

The molar Gibbs energy of the phase Spinel was expressed using the compound energy formalism derived by Hillert and Staffansson [15] and generalized by Sundman and Ågren [16] under the condition $y^{\mathrm{III}}_{\mathrm{O^{-2}}} = 1$ as follows:

$$\begin{aligned} G_m = {} & y^{\mathrm{I}}_{\mathrm{Zn^{2+}}}\, y^{\mathrm{II}}_{\mathrm{Sn^{4+}}}\, {}^{o}G_{\mathrm{Zn_2SnO_4}} + \\ & + y^{\mathrm{I}}_{\mathrm{Zn^{2+}}}\, y^{\mathrm{II}}_{\mathrm{Zn^{2+}}}\, {}^{o}G_{\mathrm{Zn_2ZnO_4[2-]}} + \\ & + y^{\mathrm{I}}_{\mathrm{In^{3+}}}\, y^{\mathrm{II}}_{\mathrm{Sn^{4+}}}\, {}^{o}G_{\mathrm{In_2SnO_4[2+]}} + \\ & + y^{\mathrm{I}}_{\mathrm{In^{3+}}}\, y^{\mathrm{II}}_{\mathrm{Zn^{2+}}}\, {}^{o}G_{\mathrm{In_2ZnO_4}} + \\ & + 2RT\left(y^{\mathrm{I}}_{\mathrm{Zn^{2+}}} \ln y^{\mathrm{I}}_{\mathrm{Zn^{2+}}} + y^{\mathrm{I}}_{\mathrm{In^{3+}}} \ln y^{\mathrm{I}}_{\mathrm{In^{3+}}}\right) + \\ & + RT\left(y^{\mathrm{II}}_{\mathrm{Sn^{4+}}} \ln y^{\mathrm{II}}_{\mathrm{Sn^{4+}}} + y^{\mathrm{II}}_{\mathrm{Zn^{2+}}} \ln y^{\mathrm{II}}_{\mathrm{Zn^{2+}}}\right) + G^{ex}_m \end{aligned} \quad (3)$$

where y^s_i represents the site fractions of sublattice component i on sublattice s. $^{\circ}G_{i:j:O^{-2}}$ are the Gibbs energy of real (Zn_2SnO_4) or hypothetical compounds where the first and second sublattices are occupied by appropriate components i and j, is the excess Gibbs energy which depends on the site fractions y^N_i and on temperature.

Bixbyite

Indium oxide In_2O_3 exists in form of two crystalline phases, the cubic form (Bixbyite type like Mn_2O_3) with Pearson symbol *cI80,* and the rhombohedral form (Corundum type like Cr_2O_3) with Pearson symbol *hR30*. The rhombohedral modification is metastable under normal

conditions, but can be produced at high temperatures and pressures [17]. In the present work this modification has been ignored. The solubility of tin in the stable form of In_2O_3 (Bixbyite) was investigated by Gonzalez and Mason [18], Ohya and Ito [19], Enoki and Echigoya [20], as well as Heward and Swenson [21] using different methods. All investigations are in general agreement and confirm a significant solubility of SnO_2 in Bixbyite. In contrast, the solubility of zinc in Bixbyite appears to be relatively small. In the ternary In_2O_3-SnO_2-ZnO system Bixbyite is enriched with tin and zinc extending toward to the composition $ZnSnO_3$ and can be described as $In_{(2-2x)}Sn_xZn_xO_3$ ($0 < x < 0.40$) [1].

Bixbyite is described in this work as solid solution phase based on In_2O_3 using the atomic sublattice model $(\underline{In}, Zn, Va)_1(\underline{In}, Sn)_1(O)_3$ assuming that the first and second sublattices can be occupied by metal atoms while the third contains oxygen atoms only. The atomic model is chosen, because the use of ions would require more additional unknown Gibbs energies to describe the solubility of tin oxide in Bixbyite. The molar Gibbs energy of this phase was expressed using the compound energy formalism [15, 16] as follows:

$$\begin{aligned} G_m = {} & y^{\mathrm{I}}_{\mathrm{In}} y^{\mathrm{II}}_{\mathrm{In}} {}^{o}G_{\mathrm{In_2O_3}} + y^{\mathrm{I}}_{\mathrm{In}} y^{\mathrm{II}}_{\mathrm{Sn}} {}^{o}G_{\mathrm{InSnO_3}} + \\ & + y^{\mathrm{I}}_{\mathrm{Zn}} y^{\mathrm{II}}_{\mathrm{In}} {}^{o}G_{\mathrm{ZnInO_3}} + y^{\mathrm{I}}_{\mathrm{Zn}} y^{\mathrm{II}}_{\mathrm{Sn}} {}^{o}G_{\mathrm{ZnSnO_3}} + \\ & + y^{\mathrm{I}}_{\mathrm{Va}} y^{\mathrm{II}}_{\mathrm{In}} {}^{o}G_{\mathrm{InO_3}} + y^{\mathrm{I}}_{\mathrm{Va}} y^{\mathrm{II}}_{\mathrm{Sn}} {}^{o}G_{\mathrm{SnO_3}} + \\ & + RT(y^{\mathrm{I}}_{\mathrm{In}} \ln y^{\mathrm{I}}_{\mathrm{In}} + y^{\mathrm{I}}_{\mathrm{Zn}} \ln y^{\mathrm{I}}_{\mathrm{Zn}} + y^{\mathrm{I}}_{\mathrm{Va}} \ln y^{\mathrm{I}}_{\mathrm{Va}}) + \\ & + RT(y^{\mathrm{II}}_{\mathrm{In}} \ln y^{\mathrm{II}}_{\mathrm{In}} + y^{\mathrm{II}}_{\mathrm{Va}} \ln y^{\mathrm{II}}_{\mathrm{Va}}) + G^{ex}_m \end{aligned} \quad (4)$$

where y^{I}_i and y^{II}_i represent the site fractions of the component i and j in the first respectively second sublattices. ${}^{o}G_{\mathrm{In_2O_3}}$ corresponds to the Gibbs energy of the indium oxide and is taken from the SGPS database [12], the Gibbs energy ${}^{o}G_{\mathrm{InO_3}}$ is estimated to be one half of the Gibbs energy of the appropriate oxide In_2O_3.

${}^{o}G_{\mathrm{ZnSnO_3}}$ is the Gibbs energy of the hypothetical compound $ZnSnO_3$, while the Gibbs energies for the also hypothetical compounds ${}^{o}G_{\mathrm{InSnO_3}}$ and ${}^{o}G_{\mathrm{ZnInO_3}}$ could be estimated using the following reciprocal equation

$$\begin{aligned} & {}^{o}G_{\mathrm{In_2O_3}} + {}^{o}G_{\mathrm{ZnSnO_3}} = \\ & = {}^{o}G_{\mathrm{InSnO_3}} + {}^{o}G_{\mathrm{ZnInO_3}} \end{aligned} \quad (5)$$

and accepting that the species on the right-hand side have identical Gibbs energies

$$\begin{aligned} & {}^{o}G_{\mathrm{InSnO_3}} = {}^{o}G_{\mathrm{ZnInO_3}} = \\ & = 0.5 \cdot {}^{o}G_{\mathrm{In_2O_3}} + 0.5 \cdot {}^{o}G_{\mathrm{ZnSnO_3}} \end{aligned} \quad (6)$$

Assessments

Thermodynamic descriptions for the binary metal systems are taken from the SGTE Solution database [13], the thermodynamic descriptions of binary metal-oxygen systems are proposed in this work. The data for the binary oxide systems In_2O_3–SnO_2, In_2O_3–ZnO and SnO_2–ZnO as well as the ternary system In_2O_3-SnO_2-ZnO are optimized using available experimental information. The calculated phase diagrams are in good agreement with the experimental data. The thermodynamic data for the ternary compounds assessed in this work are given in Table 2. The Gibbs energies of $(Me_1O_x)_A(Me_2O_y)_B$ have been based on stoichiometric combinations of Me_1O_x and Me_2O_y using a Neumann-Kopp approach. The values for ΔH^0_{298} and S^0_{298} have been assessed according to available experimental data.

The end-member Gibbs-energies $G°$ as well as the various binary and ternary

interaction parameters between species both in the liquid and solid solutions have been assessed in order to obtain correct representations of the solubility regions. The optimization of the chosen solution parameters based on the available experimental data was performed using the optimizer module OptiSage included in the FactSage software [22, 23].

Results and discussion

The metallic subsystems

As indicated above, the data for the three metallic subsystems have been taken from the SGTE Solution database [13]. The resulting binary phase diagrams as well as the ternary liquidus surface are given below for reasons of completeness.

The In–O system

The binary In-O system contains one stoichiometric compound, In_2O_3. The crystal structure of stable Indium oxide is the cubic form (Bixbyite type), whereas the rhombohedral modification (Corundum type) is metastable. According to Schneider [24], the melting point of Bixbyite In_2O_3 is 1910 ± 10 °C.

The solubility of oxygen in liquid indium was investigated first by Fitzner and Jacob [25] in the temperature range 650–820 °C using a phase equilibration technique. Later investigations using different techniques [26, 27] did not confirm these results [25]. Otsuka, Sano and Kozuka [26] determined the solubility of oxygen using coulometric titrations and later Otsuka, Kozuka and Chang [27] have used an isopiestic equilibration technique. Both measurements are in good agreement and show lower solubility of oxygen in liquid indium than determined by Fitzner and Jacob [25].

Isomäki, Hämäläinen et al. [28] in their assessment of the In-O binary system used the experimental data Fitzner and Jacob [25] applying the ionic liquid model.

Figure 5 shows the calculated phase diagram of the In-O binary system calculated from the present database compared with the experimental melting temperature of In_2O_3 [24]. Figure 6 shows the Indium-rich part of the phase diagram compared

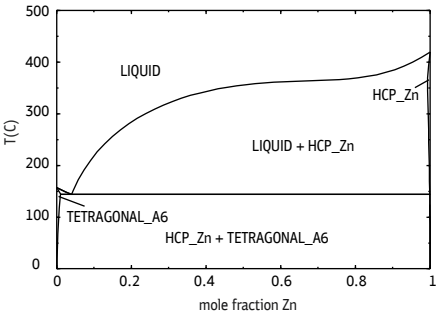

Fig. 2. Calculated In-Zn phase diagram

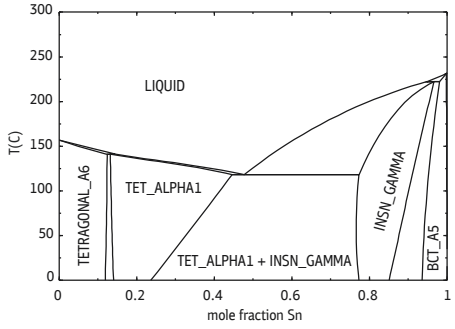

Fig. 1. Calculated In-Sn phase diagram

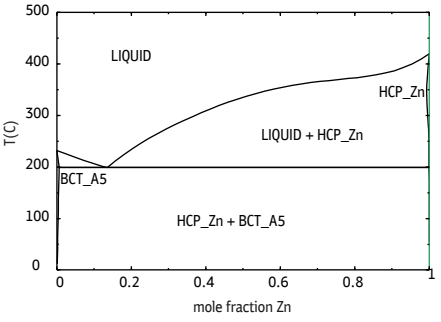

Fig. 3. Calculated Sn-Zn phase diagram

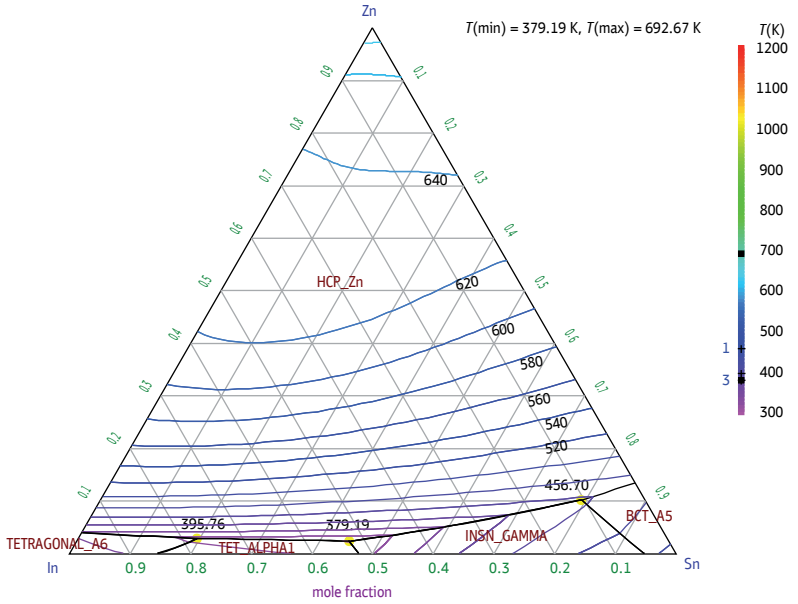

Fig. 4. Calculated liquidus surface in the In-Sn-Zn system

with the experiments [25–27], the agreement is very good.

The Sn-O system

The Sn-O phase diagram used for the optimization was taken from Massalski [17], which is based on the experimental data reported by McPherson, Hansen [29] and Spandau, Kohlmeyer [30]. The system is characterized by a large region of liquid immiscibility between pure tin and "tin oxide" — rich compositions. The monotectic reaction between metal-rich and tin oxide-rich liquid is assumed to have a temperature of 1040 °C and liquid compositions of 3.3 and 50.3 at. % O according to [17]. It was confirmed by later investigations carried out by Cahen, David et al. [31] using DSC and XRD experiments.

The Sn-O binary system contains three intermediate compounds SnO, SnO_2 and Sn_3O_4. Although the experimentally determined melting temperatures of SnO_2 vary enormously, all investigations agree that this compound melts congruently. Ac-

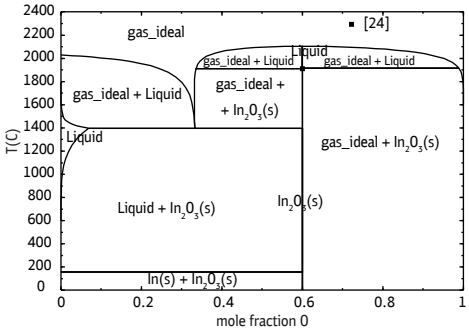

Fig. 5. Calculated In-O phase diagram

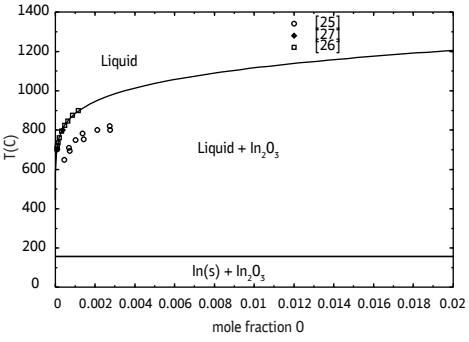

Fig. 6. Calculated phase equilibria in the In-rich part of the In–O diagram compared with experimental data [25–27]

cording to [31] this compound melts congruently at 2000 °C in contradiction to the SGPS database [12] which gives a melting temperature of 1630 °C. In the present work the thermodynamic properties of pure SnO_2 were taken from [12]. Moh [32] have reported the existence of the compound SnO which is formed by a peritectoid reaction at 270 °C (βSn) +Sn_3O_4→SnO. Sn_3O_4 is not stable at room temperature and decomposes at 450 °C [32].

A first thermodynamic assessment of the binary Sn-O system was given by Cahen, David et al. [31]. They assumed the melting temperature of SnO_2 to be 2000 °C and have modelled also the stoichiometric compounds SnO and Sn_3O_4 using the thermal stabilities experimentally determined by Moh [32]. Later, a thermodynamic assessment was carried out by Isomäki, Hämäläinen et al. [28] where the thermodynamic data for SnO_2 were taken from the SGPS database [12] with the lower melting temperature of 1630 °C. The other two compounds were not considered in this work. In both assessments, the liquid phase was described using the ionic liquid model. In the assessment by Cahen [31], the entropies of formation for the compounds SnO and SnO_2 were determined to be 96.347 J/mol·K and 183.114 J/mol·K, respectively, which is in contradiction with the values published by Barin [33] (56.48 and 52.34 J/mol·K) and also the SGPS database [12] (57.17 and 49.01 J/mol·K).

In the present work the thermodynamic data for SnO_2 were taken from the SGPS database [12]. Also, the heat capacity of the compound SnO was taken from this source. The heat of formation of SnO determined by Li-Zi et al. [34] (–285920 J/mol) was used for the optimization combined together with the phase diagram data [32]. The assessed value is –289853 J/mol, the difference to the measured value being about 1.37%. Sn_3O_4 is modeled to be stable till 450 °C according to the experimental value of 450 °C [32].

The calculated Sn–O phase diagram is presented in Figure 7 compared with available experimental information; the agreement is good.

The Zn-O system

For the binary Zn–O system no phase diagram is available. The information on this system including thermodynamics and structure of ZnO has been summarized by Wriedt [35]. The system contains one stoichiometric compound ZnO with known melting temperature (1972 °C) [17] but unknown melting behavior. No solubility of oxygen in pure zinc was reported. The binary Zn-O phase diagram resulting from the present dataset is shown in Figure 8 compared with the experimental data given in [17].

Zinc monoxide decomposes congruently by sublimation to the gaseous elements according to the following reaction: $ZnO(s) \rightleftarrows Zn(g) + 0.5O_2(g)$.

The sublimation/vaporization of zinc oxide has been investigated by Knudsen Effusion Mass-spectroscopy (KEMS) [36–39]. At temperatures below 1500 K the vapor above ZnO consists almost exclusively

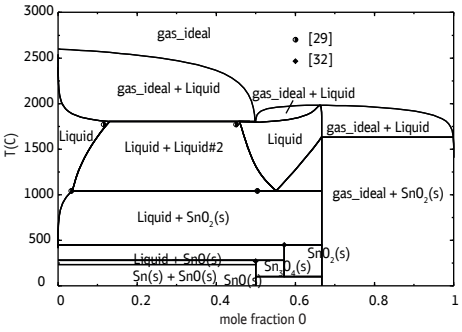

Fig. 7. Calculated Sn-O phase diagram compared with experimental data [29, 32]

of Zn atoms and O_2 molecules, which confirms the congruent vaporization of ZnO. The oxygen partial pressure, which could not be measured correctly in the experiment, was estimated in agreement with the congruent sublimation condition by the above reaction as $P(O_2) = 1/2 \cdot P(Zn)$. Under the conditions of gas phase effusion from the cell, this relation takes the form $P(O_2) = 1/2[M(O_2)/M(Zn)]^{1/2} \cdot P(Zn)$, where $M(O_2)$ and $M(Zn)$ designate the oxygen and zinc molar masses. The sublimation enthalpy can be obtained from the temperature dependence of $P(Zn)$ [38, 39] or calculated using the third-law [39]. The latter value is considered as more exact.

The selected data on the partial pressure of atomic Zn from the literature [37–41] are presented in Figure 9 (points and dashed lines) compared with the present equilibrium calculations (solid lines).

The deviation between the experimental datasets is notable especially in case of oxygen. It should be noted that the thermodynamic data for pure Zn, ZnO, O_2 were taken from the SGTE databases [11, 12] without changes. Therefore, the discrepancy can be explained by differences with respect to both the thermodynamic data of individual gaseous species and the sublimation enthalpy of ZnO. For this, a value of 465.66 kJ/mol is used in the SGPS database. It is, however, in good agreement with the literature, i.e. 461.9 (via third-law calculations in [39]) or 467.66 in [37, 38].

The Me1-Me2-O systems

Predicted isothermal sections at 500 °C for the ternary In–Sn–O, In–Zn–O and Sn–Zn–O systems are given in Figures 10–12. The pseudo-binary systems In_2O_3–SnO_2, SnO_2–ZnO and In_2O_3–ZnO are considered as a part of the corresponding systems Me1–Me2–O. It should be noted

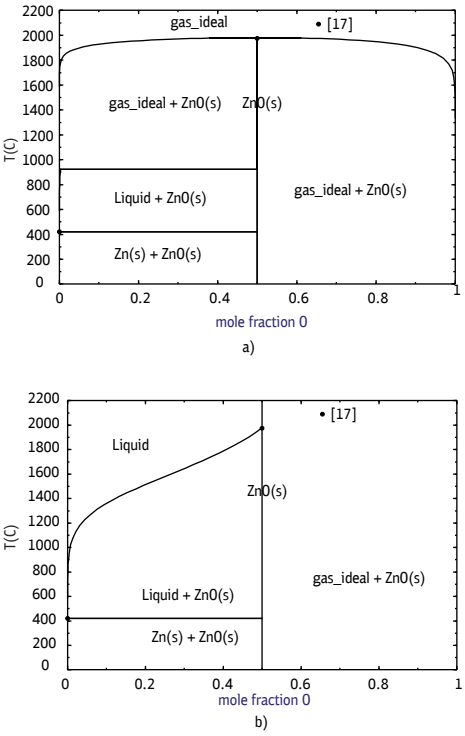

Fig. 8. Calculated Zn–O phase diagram: *a* — with participation of the gas phase, *b* — without

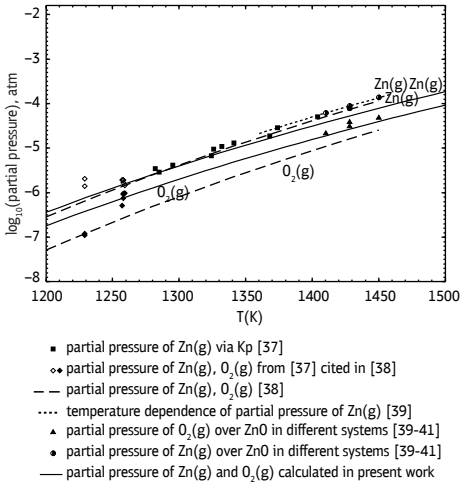

Fig. 9. Partial pressure of Zn and O_2 over ZnO: comparison of literature data (points, dashed, dotted lines) with calculations solid (lines)

that the data for the ternary metallic system In-Sn-Zn and its binary subsystems were taken from the SGTE alloy database [13] and are not given in this paper. Only in the liquid metal phase a small solubility of O is calculated from the present data.

The behaviour of the respective systems along the oxide pseudo-binary systems is discussed below.

The In_2O_3–SnO_2 system

The pseudo binary system In_2O_3–SnO_2 is characterized by the presence of two intermediate phases stable at high temperatures, a significant solubility of tin in indium oxide and a eutectic reaction close to the tin-rich side. The system was investigated by Enoki and Echigoya [20] between 1200 and 1600 °C by TEM observations. Heward and Swenson [21] studied the phase diagram in the temperature range 1000–1650 °C using electron probe microanalysis (EPMA) and X-Ray diffraction (XRD) analysis of solid-state sintered samples. The solubility ranges of tin oxide in Bixbyite solid solution were investigated by Ohya, Ito et al. [19], Gonzales and Mason [18] and Harvey [1]. The experimentally determined solubility limits and phase boundaries for the Bixbyite solid solution contradict each other. According to Heward and Swenson [21], the maximal solubility of SnO_2 in In_2O_3 was found to be 13.1 mol.% at 1650 °C, whereas Ohya [19] reported 5% at 1500 °C. In contrast, the solubility of indium in SnO_2 appears to be negligibly small [18, 21], which differs from the phase diagram obtained by Enoki [20]. In the In_2O_3-SnO_2 system two intermediate compounds, $Sn_3In_4O_{12}$ and $SnIn_2O_5$, were observed. Both are stable at high temperatures and decompose eutectoidally at 1325 and 1575 °C, respectively [21]. The stoichiometric compound $Sn_3In_4O_{12}$ was reported to be stable at temperatures above 1300 °C [18, 20] but was not observed by Harvey [3] at 1275 °C. The data on the experimentally determined thermal stability of the compound $In_4Sn_3O_{12}$ are collected in Table 4.

The In-Sn-O system has been thermodynamically modelled by Isomäki,

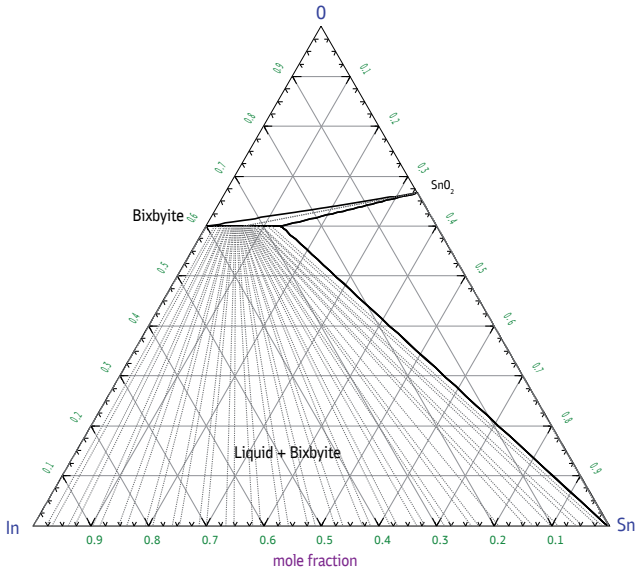

Fig. 10. The calculated In-Sn-O isothermal section at 500 °C

Hämäläinen et al. [28] who applied an ionic liquid two-sublattice model for the description of the liquid phase (Sn^{+2}, In^{+3}) (SnO_2,O^{-2},Va). Only one compound ($Sn_3In_4O_{12}$) was modeled in this work, the solubility of tin in In_2O_3 were optimized using the data of Enoki [20] which are significantly higher than those reported by Ohya

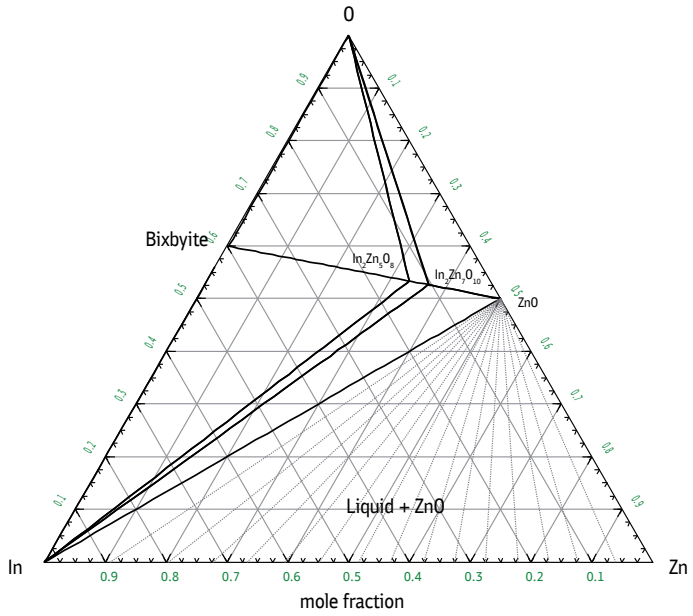

Fig. 11. The calculated In-Zn-O isothermal section at 500 °C

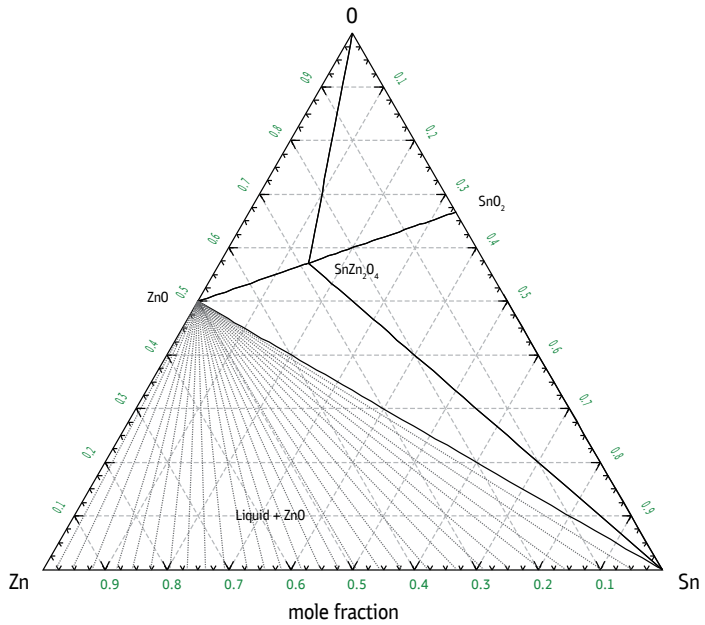

Fig. 12. The calculated Sn-Zn-O isothermal section at 500 °C

[19], Harvey [1] and Gonzalez [18]. The values by Enoki [20] were not used for the optimization in the present work. The calculated In_2O_3-SnO_2 binary system in air is presented in Figure 13 compared with the experimentally determined phase boundaries. The tin solubility in In_2O_3 increases with temperature and reaches 4.6 at. % at 1730 °C. The system contains furthermore two intermediate high-temperature compounds $Sn_3In_4O_{12}$ and $SnIn_2O_5$, the transition temperatures of which could be taken from the literature [20, 21, 42].

The calculated decomposing temperature of $Sn_3In_4O_{12}$ is 1333 °C, very close to the experimental values 1325 [21] and 1335 °C [18] while the calculated T_2-temperature (1646 °C) agrees well with the experimental data by [21] and [42].

The In_2O_3-ZnO system

In the pseudo-binary system In_2O_3-ZnO Kasper [43] found that zinc oxide and indium oxides reacted at 1100 °C with formation of a series of homologous oxides $In_2Zn_kO_{k+3}$ where k = 2–5 and 7. Based on high-resolution electron microscopy results, Cannard and Tilley [44] proposed that the structures consist of k ZnO layers separated by two $InO_{1.5}$ layers. ZnO has the wurtzite structure, In_2O_3 crystallizes in the cubic bixbyite structure, and these two structures intergrow along the hexagonal c-axis direction. According to [44], at high ZnO concentrations $In_2Zn_kO_{k+3}$ form compositions with k = 4–11 at 1100 °C. Later, Nakamura [45] and Kimizuka [46] suggested that the compounds are isostructural with $LuFeO_3(ZnO)_k$. Although the two models are not identical, both exhibit wurtzite-type layers perpendicular to the c-axis of the $In_2Zn_kO_{k+3}$ structures. Compounds with k = 3–11, 13, 15, 17, 19 were characterized by Nakamura [45, 47] using XRD and scanning electron microscopy (SEM). Moriga et al. [6] presented the sub-solidus phase diagram for the system In_2O_3-ZnO over the temperature range 1100–1400 °C. Homologous compounds $In_2Zn_kO_{k+3}$ with k = 3–7, 9, 11, 13, and 15 were reported based on XRD. At 1100 °C, $In_2Zn_5O_8$ and $In_2Zn_7O_{10}$ only were found to be stable along with ZnO and In_2O_3, whereas the number of stable compounds increased as the temperature increased.

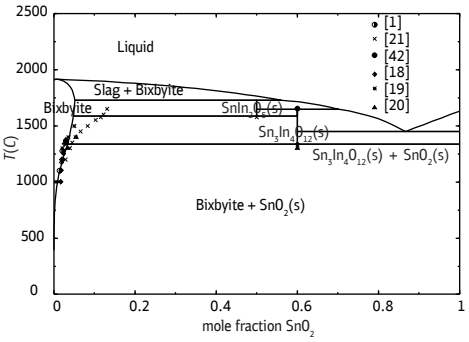

Fig. 13. The calculated In_2O_3-SnO_2 phase diagram in air compared with experimental data [1, 18–21, 42]

Table 4

Thermal stability of ternary stoichiometric compound $Sn_3In_4O_{12}$

T_1, °C	T_2, °C	T_1, °C in this work	T_2, °C in this work
1300 Enoki [20]	–	1333	1646
1365 Ohya [19]	–		
1335 Gonzalez [18]	–		
1325 Heward [21]	1650 Heward [21]		
–	1652 Bates [42]		

The temperature ranges of stability determined in [6] agree with the previously reported information [43, 45, 46]. The difference was that the compounds with k = 4 and 8 were not observed by Moriga [6] over the temperature range studied. Moreover, the presence of the compound with k = 15 of the $In_2Zn_kO_{k+3}$ series was almost impossible to detect with the XRD technique used in [6]. The formation of homologues series $In_2Zn_kO_{k+3}$ (where k = 3–7, 9, 11) was confirmed at 1275 °C in the study on the ternary system In_2O_3–SnO_2–ZnO [1], while the compounds with k = 6, 13, 15 became stable at higher temperatures. The lattice constant, microstructure and electrical characteristics of In_2O_3 ceramic doped by ZnO were investigated by Park et al. [48]. The solubility limit of ZnO in In_2O_3 was reported to be close to 1 at.% when IZO (indium zinc oxide) was sintered in oxygen atmosphere. Sintering in nitrogen decreased the solubility limit to below 1 at.%.

No previous assessments on the system In_2O_3–ZnO were found in the literature. The present description of the system In_2O_3–ZnO is based on the data reported by Moriga [6]. The series of phases with the general formula $In_2Zn_kO_{k+3}$ with k = 3–7, 9, 11, 13, 15 was modelled in form of stoichiometric oxides. The thermodynamic data of these compounds are given in Table 2. Heat capacities of these compounds were generated according to Neumann — Kopps rule based on the component oxides; the enthalpies and entropies of formation were optimized in accordance with the stability ranges of the phases. The formation enthalpy for the compounds with k = 5 and 7 optimized in the present work are in very good agreement with those reported in [41] as shown in Figure 14. The literature data have been derived from a vaporization study of the system In_2O_3–ZnO with the KEMS technique. It is worth noting that all compounds show a very consistent trend with increasing content of Sn.

The solubility limit of ZnO in In_2O_3 (bixbyite phase) was calculated at 1.56 mol.% and 1698 °C using the following atom-based model description of the phase: $(\underline{In}, Zn, Va)_1(\underline{In}, Sn)_1(O)_3$. The liquid phase is assumed to consist of the component oxides, Zn_2O_2 and In_2O_3, i.e. following the rule of two cations per molecule. The Gibbs energies of the stoichiometric homologous compounds are summarized in Table 2. The calculated phase diagram for the system In_2O_3–ZnO

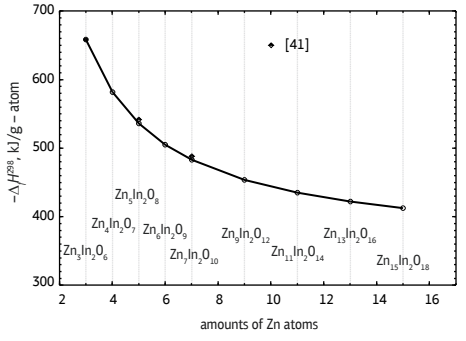

Fig. 14. Heat of formation of the stoichiometric compounds in the In_2O_3–ZnO system

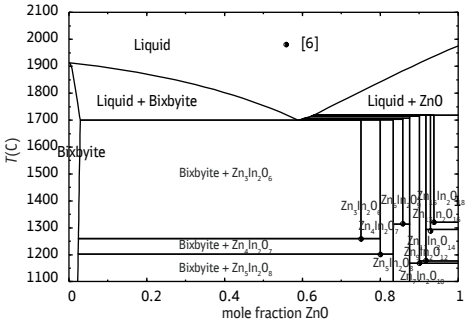

Fig. 15. The calculated In_2O_3–ZnO phase diagram in air compared with experimental data [6]

is presented in Fig. 15 compared with the experimental data [6].

The SnO_2-ZnO system

Enoki [49] proposed a preliminary phase diagram for the system SnO_2–ZnO with the spinel phase only. The oxide mixtures were equilibrated at 1200 and 1400 °C and characterized by XRD. Most of the experimental studies [4, 49, 50] on this system agreed that there is one stable compound with the composition $SnZn_2O_4$. This compound has inverse spinel structure and can be obtained by solid state reaction from the component oxides or by decomposition of the salts zinc acetate ($Zn(CH_3COO)_2$ and tin tetrachloride ($SnCl_4$). In contrast, the information on the second phase, $ZnSnO_3$, is contradictory. Shen and Zhang [51] reported that this compound has a perovskite structure, whereas Inagaki [52] proposed an ilmenite structure which is more reasonable due to the fact that the ionic radius of Zn^{2+} radius is too small to form a stable perovskite structure as has been confirmed later by Kovacheva and Petrov [53].

Palmer and Poeppelmeier [4] studied sub-solidus phase equilibria in the system Ga_2O_3–SnO_2–ZnO at 1250 °C using solid state synthesis and XRD. The ZnO–SnO_2 binary system contains one intermediate compound, $SnZn_2O_4$ with two-phase regions between the end-members and the spinel. According to [4], the lattice parameters of $SnZn_2O_4$ were unchanged (from the nominal value) in two-phase mixtures with ZnO or SnO_2, indicating minimal solubility of either oxide into the spinel phase. Hansson et al. [50] investigated phase equilibria for SnO_2-ZnO system in air in the temperature range 1200 to 1400 °C using high-temperature equilibration and quenching techniques followed by electron probe X-ray microanalysis (EPMA). The maximum solubility of ZnO in SnO_2 was found to be approximately 1.5 mol.% in the range of conditions investigated. The concentration of tin oxide in zincite (ZnO) is negligible between 1300 and 1400 °C in air within the limits of experimental uncertainty. A slight solubility of ZnO in the stoichiometric $SnZn_2O_4$ spinel can be observed at all temperatures. Later Harvey et al. [1] did not observe a change of lattice parameter between pure ZnO or pure SnO_2 and doped compositions. Mihaiu et al. [54] undertook a systematic study of the phase formation over the whole compositional range of the ZnO-SnO_2 binary system in the temperature range 500–1500 °C. Starting with 900 °C, the formation of the $SnZn_2O_4$ with inverse spinel type structure was found in all samples. The formation of the $ZnSnO_3$ was not observed under the experimental conditions used. In the temperature ranges 1000–1500 °C, no change in the phase composition was observed.

Vaporization processes in the ZnO–SnO_2 system have been studied by the Knudsen effusion technique in combination with mass spectrometric analysis (KEMS) of the vapor phase in the temperature range 1360 K to 1460 K [39]. Complete isothermal sublimation experiments have been performed to determine the partial pressures of vapor components over the whole system. The elemental composition of samples was quantified using laser mass spectrometry. By isothermal sublimation, the change of partial pressure of Zn over the system is caused by phase transformations in the solid state from pure ZnO through two heterogeneous fields (ZnO + Zn_2SnO_4 and Zn_2SnO_4 + SnO_2) to pure tin oxide. It has been found that the gas phase mainly consists of Zn(g), O_2 and SnO(g). The partial pressures of the vapor species were determined at 1450 K.

In the present work, the compound $SnZn_2O_4$ is treated as stoichiometric according to [3, 6] and calculated to be stable up to its melting point of 1675 °C. This compound is considered as the end-member constituent in the Spinel phase for the ternary system. The heat capacity of $SnZn_2O_4$ was based on the data of the component oxides according to Neumann-Kopp (Table 2), the standard enthalpy of formation was optimized based on the experimental value from Gribchenkova [39]. The entropy was adjusted in order to represent the melting point of spinel. The compound $ZnSnO_3$ was omitted from consideration according to literature data on its instability [39].

The liquid phase in the system SnO_2–ZnO includes the associate $SnZn_2O_4$/1.5 along with the basic oxides according to the modified associate species model. The melting properties of the spinel compound were based on those for liquid oxides. The two eutectics (Spinel and ZnO as well as Spinel and SnO_2) are calculated at 1647 and 1425 °C, respectively. The calculated phase diagram of the system SnO_2-ZnO is given in Figure 16.

The calculated activities across the system SnO_2–ZnO at 1450 K are compared in Figure 17 with those measured in [39] using KEMS. The thermodynamic data on the gas phase are taken from the SGPS database [12]. The following main gas species are found by calculation of equilibrium between the condensed phases and gas – Zn, SnO and O_2.

The ratio between these species agreed with the measurements [39]; however, the absolute values of the partial pressures (especially for Zn) differ from the experimental data due to scattering of experimental data on *P*(Zn) obtained by using such a complicated method as KEMS. Moreover, the disagreement can be explained by possible small inconsistencies concerning the thermodynamic data of the gas components in the SGTE database, as was already mentioned above regarding the Zn–O system.

The In_2O_3-SnO_2-ZnO system

The ternary In_2O_3-SnO_2-ZnO system does not exhibit any ternary compounds, but presents two significant solid solution phases, the $SnZn_2O_4$ Spinel phase enriched with indium with the formula $Zn_{(2-x)}Sn_{(1-x)}In_{2x}O_4$ and the Bixbyite solid solution based on In_2O_3 and extending far toward the $SnZnO_3$ composition with the formula $In_{(2-2x)}Sn_xZn_xO_3$. Palmer, Poeppelmeier and Mason [55] studied the solid solubility of ZnO and SnO_2 in Bixbyite at 1100 and 1250 °C using X-ray diffraction and determined a very strong coupled

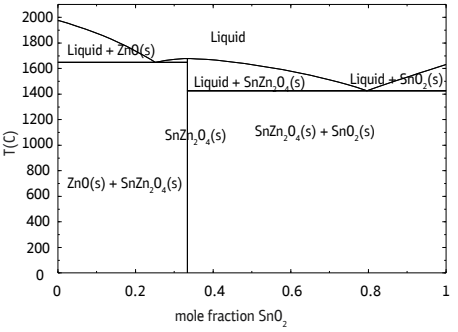

Fig. 16. Calculated SnO_2–ZnO phase diagram in air

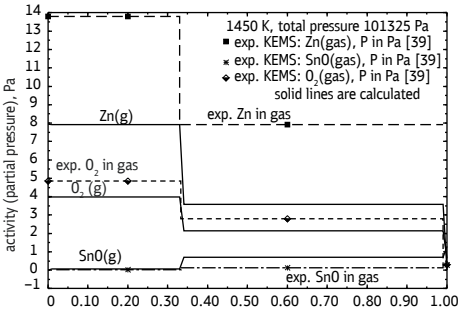

Fig. 17. Calculated and experimental activities in SnO_2–ZnO system at 1450 K

solubility of SnO_2 and ZnO. The maximum combined solubility of Zn and Sn can reach 40 cation %, the resulting material at this point can be described as $In_{1.2}Sn_{0.4}Zn_{0.4}O_3$. Later investigations by Kammler et al. [56] using X-ray powder diffraction confirmed high solubility of zinc and tin in In_2O_3 at 1250 °C. Kammler reported also a wide spinel solution range, $Zn_{2-x}Sn_{1-x}In_{2x}O_4$ ($0 < x < 0.45$) and also a significant solubility of tin in $Zn_3In_2O_6$ which was, however, not confirmed by later investigations [1, 2]. The phase diagram data published in [56] are constructed schematically and were not used for the present optimization work.

The present assessment of the ternary system is mainly based on the phase equilibria data published in [1]. Harvey, Poeppelmeier and Mason [3] investigated the subsolidus phase relationships at 1275 °C using X-ray diffraction. They reported the existence of two extended solid solutions and preliminary phase relations between them and other coexisting compounds. Both solid solution phases exhibit constant Zn:Sn ratio and appear on the phase diagram as long vertical lines. The one significant solid solution phase is Bixbyite In_2O_3, enriched by tin and zinc, where up to 40% of indium can be replaced by tin and zinc. According to Harvey [1], the Bixbyite phase can be described using the formula $In_{(2-2x)}Sn_xZn_xO_3$, where x can reach a maximum of 0.4. At 1275 °C, Bixbyite is in general in equilibrium with the Spinel phase, compound $(ZnO)_k(In_2O_3)$, where k = 3, and also with the tin oxide SnO_2. The other important solid solution phase reported by Harvey [1] is the Spinel phase, which extends from the binary composition $SnZn_2O_4$ towards the In_2ZnO_4 composition. Harvey confirmed Spinel phase boundaries and formula experimentally found by Kammler [56] to describe this indium-doped Spinel as $Zn_{(2-x)}Sn_{(1-x)}In_{2x}O_4$,($0 < x \leq 0.45$), whereby at $x = 0.45$ the Spinel composition corresponds to the formula $Zn_{1.55}Sn_{0.55}In_{0.90}O_4$. Harvey investigated also very intensively a zinc-oxide-rich region at 1275 °C and corresponding phase equilibria. As mentioned before, along the binary ZnO-In_2O_3 edge at 1275 °C there is a series of homologous compounds $(ZnO)_k(In_2O_3)$ (where k = 3–5, 7, 9, 11), all of which are in equilibrium with the phase Spinel, starting with the first one $(ZnO)_{11}(In_2O_3)$ and finishing with the last $(ZnO)_3(In_2O_3)$ which is in equilibrium with Spinel maximally enriched in indium. The compounds with k > 11 were not found in equilibrium with spinel at 1275 °C due to sluggish kinetics in the ZnO-rich composition range [1].

Figure 18 shows the calculated isothermal section at 1275 °C in the $InO_{1.5}$–SnO_2–ZnO system in air compared with experimental data [1]. The experimentally determined extensions of the solid solution phases Bixbyite and Spinel, the two-phase regions and also the compatibility triangles could be reproduced satisfactorily by the calculations.

Conclusions

A thermodynamic dataset containing all phases in the system In_2O_3-SnO_2-ZnO has been generated using the available experimental information (phase diagrams, phase transitions, structure, enthalpies of formation). The liquid and solid phases have been introduced into the thermodynamic description, solid solution phases such as Spinel and Bixbyite have been modelled using the multi-sublattice approach. Fourteen stoichiometric compounds have also been thermodynamically assessed. The

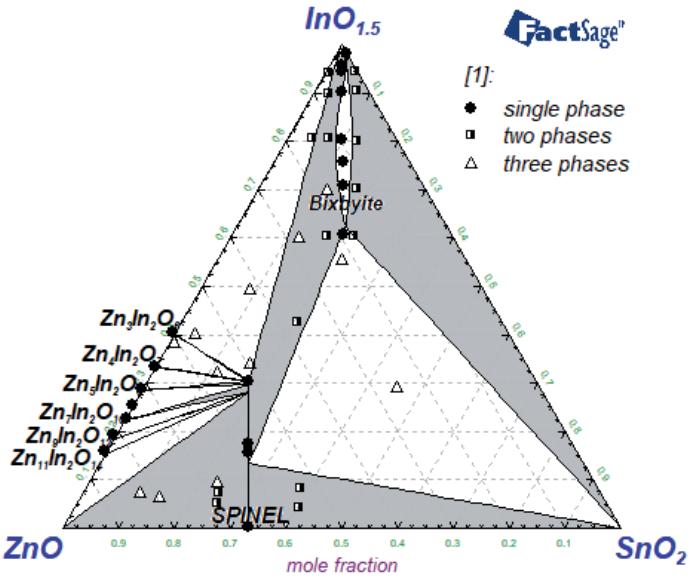

Fig. 18. Subsolidus phase relationships in In_20_3-SnO_2-ZnO system in air at 1275 °C and 1 atm compared with experimental data [1]. Grey areas are the two-phase regions

liquid species tin (II, IV) oxides, indium and zinc oxides and the binary associate species ($SnZn_2O_4$) have been introduced to the non-ideal associate solution. The general agreement between the calculated phase equilibria as well as thermodynamic properties and the respective experimental data is good. The dataset can be applied to studies on the formation of ZITO-based TCOs.

References

1. Harvey SP, Poeppelmeier KR, Mason TO. Subsolidus Phase Relationships in the ZnO–In_2O_3–SnO_2 System. Journal of the American Ceramic Society. 2008;91(11):3683–9. DOI: 10.1111/j1551–2916.2008.02686.x.
2. Hoel CA, Mason TO, Gaillard J-F, Poeppelmeier KR. Transparent Conducting Oxides in the ZnO-In_2O_3-SnO_2 System. Chemistry of Materials. 2010;22(12):3569–79. DOI: 10.1021/cm1004592.
3. Granqvist CG, Hultåker A. Transparent and conducting ITO films: new developments and applications. Thin Solid Films. 2002;411(1):1–5. DOI: 10.1016/S0040-6090(02)00163–3.
4. Palmer GB, Poeppelmeier KR. Phase relations, transparency and conductivity in Ga_2O_3-SnO_2-ZnO. Solid State Sciences. 2002;4(3):317–22. DOI: 10.1016/S1293-2558(01)01258–4.
5. Minami T, Kakumu T, Takata S. Preparation of transparent and conductive In_2O_3–ZnO films by radio frequency magnetron sputtering. J Vac Sci Technol. 1996;A14:1704–8. DOI: 10.1116/1.580323.

6. Moriga T, Edwards DD, Mason TO, Palmer GB, Poeppelmeier KR, Schindler JL, et al. Phase Relationships and Physical Properties of Homologous Compounds in the Zinc Oxide-Indium Oxide System. Journal of the American Ceramic Society. 1998;81(5):1310–6. DOI: 10.1111/j.1151–2916.1998.tb02483.x .
7. Besmann TM, Spear KE. Thermodynamic modelling of oxide glasses. J Am Ceram Soc. 2002;85(12):2887–94. DOI: 10.1111/j.1151–2916.2002.tb00552.x.
8. Yazhenskikh E, Jantzen T, Hack K, Müller M. Critical thermodynamic evaluation of oxide system relevant to fuel ashes and slags: Potassium oxide-magnesium oxide-silica. Calphad. 2014;47:35–49. DOI: 10.1016/j.calphad.2014.05.006.
9. Jantzen T, Hack K, Yazhenskikh E, Müller M. Evaluation of thermodynamic data and phase equilibria in the system Ca-Cr-Cu-Fe-Mg-Mn-S Part II: Ternary and quasi-ternary subsystems. Calphad. 2017;56:286–302. DOI: 10.1016/j.calphad.2017.01.007.
10. Jantzen T, Hack K, Yazhenskikh E, Müller M. Addition of TiO_2 and Ti_2O_3 to the Al_2O_3-FeO-Fe_2O_3-MgO system. Calphad. 2018;62:187–200. DOI: 10.1016/j.calphad.2018.05.009.
11. SGTE unary database 2017.
12. SGPS — SGTE pure substances database (v13.1) 2017.
13. SGTE Solution database 2017.
14. Pearson WB. A Handbook of Lattice Spacings and Structures of Metals and Alloys. Oxford: Pergamon Press; 1967.
15. Hillert M, Staffansson L–I. Regular Solution Model for Stoichiometric Phases and Ionic Melts. Acta Chem Scand. 1970;24(10):3618–26. DOI:10.3891/acta.chem.scand. 24–3618.
16. Sundman B, Aagren J. A regular solution model for phases with several components and sublattices, suitable for computer applications. J Phys Chem Solids. 1981;42(Copyright (C) 2018 American Chemical Society (ACS). All Rights Reserved.):297–301. DOI: 10.1016/0022–3697(81)90144-x.
17. Massalski TB. Binary Alloy Phase Diagrams. Second ed. Metals Park, OH ASM International; 1990.
18. González GB, Mason TO, Okasinski JS, Buslaps T, Honkimäki V. Determination of the Solubility of Tin in Indium Oxide Using In Situ and Ex Situ X-Ray Diffraction. J Am Ceram Soc. 2011:1–7. DOI: 10.1111/j.1551–2916.2011.04999.x.
19. Ohya Y, Ito T, Kaneko M, Takahashi Y. Solid solubility of SnO_2 in In_2O_3. J Ceram Soc Jpn. 2000;108(9):803–6. DOI: 10.2109/jcersj.108.1261_803.
20. Enoki H, Echigoya J, Suto H. The intermediate compound in the In_2O_3-SnO_2 system. Journal of Materials Science. 1991;26(15):4110–5. DOI: 10.1007/bf02402954.
21. Heward WJ, Swenson DJ. Phase equilibria in the pseudo-binary In_2O_3-SnO_2 system. J Mater Sci. 2007;42(Copyright (C) 2018 American Chemical Society (ACS). All Rights Reserved.):7135–40. DOI: 10.1007/s10853-007-1569-y.
22. FactSage: Facility for the Analysis of Chemichal Thermodynamics. Montreal, Canada: CRCT-ThermFact Inc. and GTT-Technologies; 1976–2015; Available from: http://www.factsage.com/.

23. Bale CW, Bélisle E, Chartrand P, Decterov SA, Eriksson G, Gheribi AE, et al. FactSage thermochemical software and databases, 2010–2016. Calphad. 2016;54:35–53. http://dx.doi.org/10.1016/j.calphad.2016.05.002.
24. Schneider SJ. Phase Equilibria in Systems Involving the Rare Earth Oxides. Part III. The Eu_2O_3-In_2O_3 System. J Res Nat Bureau of Standards. 1961;65A(5):429–34. DOI: 10.6028/jres.065A.044.
25. Fitzner K, Jacob KT. Solubility and activity of oxygen in liquid indium and copper-indium alloys. Journal of the Less Common Metals. 1977;52(2):279–91. DOI: 10.1016/0022–5088(77)90009–1.
26. Otsuka S, Sano T, Kozuka Z. Activities of oxygen in liquid thallium and indium from electrochemical measurements. MTB. 1980;11(2):313–9. DOI: 10.1007/bf02668417.
27. Otsuka S, Kozuka Z, Chang YA. Oxygen solubility in liquid indium and oxygen diffusivity in liquid indium and tin. MTB. 1984;15(2):329–35. DOI: 10.1007/bf02667336.
28. Isomäki I, Hämäläinen M, Gierlotka W, Onderka B, Fitzner K. Thermodynamic evaluation of the In–Sn–O system. Journal of Alloys and Compounds. 2006;422(1):173–7. DOI:10.1016/j.jallcom.2005.11.083.
29. McPherson DJ, Hansen M. The system Zirconium-Tin. Trans ASM. 1953;45:915–33.
30. Spandau H, Kohlmeyer EJ. Uber Zinnmonoxyd und sein Verhalten bei hohen Temperaturen. Z Anorg Chem. 1947;254:65–82.
31. Cahen S, David N, Fiorani JM, Maître A, Vilasi M. Thermodynamic modelling of the O–Sn system. Thermochimica Acta. 2003;403(2):275–85. DOI: 10.1016/S0040-6031(03)00059–5.
32. Moh GH. Tin-containing mineral systems. I. Tin-iron-sulfur-oxygen system and mineral assemblages in ores. Chem Erde. 1974;33(Copyright (C) 2018 American Chemical Society (ACS). All Rights Reserved.):243–75.
33. Barin I. Thermochemical Data of Pure Substances: VCH Verlagsgeselschaft mbH; 1995.
34. Li-Zi Y, Zhi-Tong S, Chan-Zheng W. A Thermodynamic Study of Tin Oxides by Coulometric Titration. Journal of Solid State Chemistry. 1994;113(2):221–4. DOI: 10.1006/jssc.1994.1363.
35. Wriedt HA. The O–Zn (Oxygen-Zinc) system. Journal of Phase Equilibria. 1987;8(2):166. DOI: 10.1007/bf02873202.
36. Searcy AW. High-Temperature Inorganic Chemistry. Progress in Inorganic Chemistry1962. DOI: 10.1002/9780470166048.ch2.
37. Anthrop DF, Searcy AW. Sublimation and Thermodynamic Properties of Zinc Oxide. J Phys Chem. 1964;68(8):2335–42. DOI: 10.1021/j100790a052.
38. Kazenas EK, Tsvetkov JV. The evaporation of oxides. Moscow: Nauka; 1997.
39. Gribchenkova NA, Steblevsky AV, Alikhanyan AS. Vaporization thermodynamics of the ZnO–SnO_2 system. The Journal of Chemical Thermodynamics. 2014;70:203–6. DOI: 10.1016/j.jct.2013.11.010.
40. Gribchenkova NA, Steblevsky AV, Alikhanyan AS. Vaporization in the Ga_2O_3–ZnO system by high temperature mass spectrometry. The Journal of Chemical Thermodynamics. 2017;115:1–6. DOI: 10.1016/j.jct.2017.07.009.

41. Gribchenkova NA, Alikhanyan AS, editors. Mass spectrometric investigation of phase equilibria and thermodynamics of ZnO-M_xO_y (M_xO_y = Ga_2O_3, In_2O_3, SnO_2) quasi-binary oxide systems. Knudsen Effusion Mass Spectrometry, KEMS Workshop; 2017 October, 23–25; Jülich, Germany: Forschungszentrum Jülich.
42. Bates JL, Griffin CW, Marchant DD, Garnier JE. Electrical conductivity, Seebeck coefficient, and structure of indium(III) oxide-tin(IV) oxide. Am Ceram Soc Bull. 1986;65:673–8.
43. Kasper H. Neuartige Phasen mit wurtzitähnlichen Strukturen im System ZnO-In_2O_3. Zeitschrift für anorganische und allgemeine Chemie. 1967;349(3-4):113–23. DOI: 10.1002/zaac.19673490302.
44. Cannard PJ, Tilley RJD. New intergrowth phases in the ZnO-In_2O_3 system. Journal of Solid State Chemistry. 1988;73(2):418–26. DOI: 10.1016/0022–4596(88)90127–2.
45. Nakamura M, Kimizuka N, Mohri T. The phase relations in the In_2O_3-Fe_2ZnO_4-ZnO system at 1350°C. Journal of Solid State Chemistry. 1990;86(1):16–40. DOI: 10.1016/0022–4596(90)90110-J.
46. Kimizuka N, Isobe M, Nakamura M. Syntheses and Single-Crystal Data of Homologous Compounds, In_2O_3(ZnO)m (m = 3, 4, and 5), $InGaO_3(ZnO)_3$, and Ga_2O_3(ZnO) m (m = 7, 8, 9, and 16) in the In_2O_3-$ZnGa_2O_4$-ZnO System. Journal of Solid State Chemistry. 1995;116(1):170–8. DOI: 10.1006/jssc.1995.1198.
47. Nakamura M, Kimizuka N, Mohri T, Isobe M. The Phase Relations in the In_2O_3-Al_2ZnO_4-ZnO System at 1350°C. Journal of Solid State Chemistry. 1993;105(2):535–49. DOI: 10.1006/jssc.1993.1246.
48. Park D-H, Son K-Y, Lee J-H, Kim J-J, Lee J-S. Effect of ZnO addition in In_2O_3 ceramics: defect chemistry and sintering behavior. Solid State Ionics. 2004;172(1):431–4. DOI: 10.1016/j.ssi.2004.03.029.
49. Enoki H. Oxide transparent electrode materials. Materia. 1995;34(3):344–51. DOI: 10.2320/materia.34.344.
50. Hansson R, Hayes PC, Jak E. Experimental study of phase equilibria in the Fe–Sn–Zn–O system in air. Can Metall Q. 2004;43(4):545–54. DOI: 10.1179/cmq.2004.43.4.545.
51. Yu-Sheng S, Tian-Shu Z. Preparation, structure and gas-sensing properties of ultramicro $ZnSnO_3$ powder. Sensors and Actuators B: Chemical. 1993;12(1):5–9. DOI: 10.1016/0925–4005(93)85003-S.
52. Inagaki M, Kuroishi T, Yamashita Y, Urata M. Syntheses of $MSn(OH)_6$ by coprecipitation and of $MSnO_3$ by thermal decomposition (M = Mg, Co, Zn, Mn, Cd, Ca, Sr, Ba). Zeitschrift für anorganische und allgemeine Chemie. 1985;527(8):193–202. DOI: 10.1002/zaac.19855270822.
53. Kovacheva D, Petrov K. Preparation of crystalline $ZnSnO_3$ from Li_2SnO_3 by low-temperature ion exchange. Solid State Ionics. 1998;109(3):327–32. DOI: 10.1016/S0167-2738(97)00507–9.
54. Mihaiu S, Atkinson I, Mocioiu O, Toader A, Tenea E, Zaharescu M. Phase formation mechanism in the ZnO-SnO_2 binary system. Rev Roum Chim. 2011;56(5):465–72.
55. Palmer GB, Poeppelmeier KR, Mason TO. Conductivity and Transparency of ZnO/SnO_2-Cosubstituted In_2O_3. Chem Mater. 1997;9 (Copyright (C) 2018 American Chemical Society (ACS). All Rights Reserved.):3121–6. DOI: 10.1021/cm9704037.

56. Kammler DR, Edwards DD, Ingram BJ, Mason TO, Palmer GB, Ambrosini A, et al. Novel Compound and Solid-Solution Transparent Conducting Oxides for Photovoltaics. In: V. K. Kapur RDM, D. Carlson, G. P. Ceasar, A. Rohatgi, editor. Electrochem Soc 195th Meeting: Photovoltaics for the 21st Century; Seattle, Washington. Pennington, New Jersey: The Electrochemical Society, Inc., 1999. P. 68–77.

Mikhaylovskaya Z. A., Buyanova E. S., Petrova S. A., Nikitina A. A.
Chimica Techno Acta. 2018. Vol. 5, No. 4. P. 189–195.
ISSN 2409–5613

DOI: 10.15826/chimtech.2018.5.4.03

Z. A. Mikhaylovskaya[a*], E. S. Buyanova[a], S. A. Petrova[b], A. A. Nikitina[a]

[a] *Ural Federal University, 19 Mira St., Ekaterinburg, 620002, Russia*
[b] *Institute for Metallurgy, Ural Branch of the Russian Academy of Sciences, 101 Amundsen St., Ekaterinburg, 620016, Russia*
E-mail: zozoikina@mail.ru

Sheelite-related strontium molybdates: synthesis and characterization

The present research is devoted to the cationic-deficient $SrMoO_4$-based sheelite-related complex oxides. The doping with bismuth to A sublattice and codoping with bismuth and vanadium (to A and B sublattices, respectively) were discussed. The X-Ray powder diffraction and infrared spectroscopy were used to investigate structural characteristics of the complex oxides. In $Sr_{1-1.5x}Bi_xMoO_4$, a superstructural ordering was observed. Conductivity and dielectric loss of ceramic samples are measured using alternating current.

Keywords: sheelite; strontium molybdates; dielectric materials.

Received: 25.10.2018. Accepted: 17.12.2018. Published: 31.12.2018.

Introduction

Scheelite-type complex oxides are quite interesting research objects because flexibility of substitutions in these systems leads to variety of their compositions, structure types and properties. Ideal scheelite-related oxides have a general formula ABO_4 and consist of A^{n+} cations and $(BO_4)^{n-}$ anions. A-site ions are coordinated with eight oxygen ions, and B-site ions are coordinated with four oxygen ion. Each site can be occupied simultaneously by different ions with various oxidation states; additional interstitial positions and vacancies lead to the deviation from the general formula. A lot of scheelite-type complex oxides are used as materials for scintillation detectors, lasers [1, 2], ionic conductors [3], phosphors [4], photocatalysts [5], and microwave dielectrics [6]. The regulation of the desired properties of sheelite-related materials can be provided by varying the quantity of the dopant, its nature, the ratios between dopants and the presence of additional vacancies or interstitial positions in the structure. For example, a substitution of A-site ions with Me^{+3} in ABO_4 complex oxide can be described in two ways: (1) a formation of $A_{1-x}Me^{+3}{}_xBO_{4+x/2}$ phases, where electroneutrality is provided by the interstitial oxygen ions; (2) a formation of $A^{+2}{}_{1-1.5x}Me^{+3}{}_x\Phi_{0.5x}MoO_4$ (or $A^{+2}{}_{1-1.5x}Me^{+3}{}_xMoO_4$) phases containing cationic vacancies Φ. The first way of substitution was detected for $Pb(Mo/W)O_4$ [7, 8] and $Ca(Mo/W)O_4$ [9] parent compounds. The second way was described for rare-earth substituted $Ca(Mo/W)O_4$, $Sr(Mo/W)O_4$ and $Cd(Mo/W)O_4$ [10–12].

As a result, cationic vacancies Φ and their ordering are additional structural factors influencing physico-chemical properties. Another way of the substitution of A positions is codoping with Me^{+3} and Me^{+1} or Me^{+5} ions, which leads to the formulae $A_{1-x}\ Me^{+1}_{0.5x}Me^{+3}_{0.5x}BO_4$ [13] and $A_{1-x}Me^{+3}_{x}B_{1-x}Me^{+5}_{x}O_4$, respectively [14]. The present research is devoted to the Bi-doped strontium molybdate $SrMoO_4$. The existence of $Sr_{1-1.5x}Bi_xMoO_4$ series was shown by Sleight and coauthors [15], who synthesized the complex oxide $Sr_{0.88}Bi_{0.08}MoO_4$ (tetragonal symmetry, Sp. Gr. $I4_1/a$) and described its good catalytic properties [15]. $Sr_{1-1.5x}Bi_xMoO_4$ family has not been described yet, while Bi-doped calcium molybdates have been intensively researched as microwave dielectric [16] or pigments [14]. The basic characteristic and structure types of $SrMoO_4$ are similar to those of $CaMoO_4$, so the Bi-doped strontium molybdates should possess similarly promising properties. In addition, Bi-doping of strontium molybdates is expected to lead to decrease of the unit cell, resulting from the significant changes in B-sublattice. Therefore, the objects of the present work are $Sr_{1-1.5x}Bi_xMoO_4$, $Sr_{1-x}Bi_xMo_{1-x}V_xO_4$, $Sr_{1-1.5x}Bi_xMo_{1-y}V_yO_{4-d}$ solid solutions and their structure and properties.

Experimental

Synthesis of $Sr_{1-1.5x}Bi_xMoO_4$ ($0 \le x \le 0.45$), $Sr_{1-x}Bi_xMo_{1-x}V_xO_4$ ($0 \le x \le 0.4$), $Sr_{1-1.5x}Bi_xMo_{1-y}V_yO_{4-d}$ ($0 < x \le 0.4, 0 < y \le 0.2$) were synthesised by conventional solid state methods from $SrCO_3$ (98.5%), Bi_2O_3 (99.9%), V_2O_5 (98.5%) and MoO_3 (99.0%). Stoichiometric amounts of dried precursors were weighed and mixed in an agate mortar as dispersion in ethanol. Mixtured powders were pelletized and heated at 550–650 °C with regrinding and repelletizing. Time of each heating was ~10 hours, the total time of heating was ~30 hours.

X-ray powder diffraction data were obtained on a DRON-3 with Cu Kα monochromatic radiation in the range of 5–75° of 2θ. IR FT spectrometry measurements were carried out at Nicolet 6700 with attenuated total reflection attachment. Density of powder samples was measured by hydrostatic weighting. For conductivity measurements, the ceramic pellets of 10 mm in diameter and *ca*. 2.5 mm thickness were covered by Pt. Impedance spectra were obtained in two-electrode measurement cell on LCR-819 and Elins Z-3000 impedance spectrometers, over the frequency ranges 1 Hz and 3 MHz to 10 Hz, respectively, at stabilised temperatures from *ca*. 25 °C to *ca*. 625 °C. Data presented correspond to the second cooling run. Data were modelled using equivalent electrical circuits with the Zview software (Version 2.6b, Scribner Associates, Inc.).

Results and discussion

Synthesis of $Sr_{1-1.5x}Bi_xMoO_4$ yielded samples with the structure of $Sr_{0.88}Bi_{0.08}MoO_4$ [15], up to $x = 0.2$ (Sp.gr. $I4_1/a$). At $0.2 < x < 0.4$ additional peaks in the small angle range are evident; for the $x > 0.45$ composition additional peaks in the pattern can be identified as Bi_3MoO_{12}. We supposed that $0.2 < x \le 0.4$ compositions have superstructural ordering caused by ordering of cationic vacancies (Fig. 1).

As a result, in the XRPD data for $0.2 < x \le 0.4$ compositions all peaks can be successfully indexed using a tetragonally ordered supercell $a_{sup}=\sqrt{5}a_{sub}$,

$c_{sup} = c_{sub}$ (where sup and sub subscripts denote the super- and subcell, respectively) in $I4_1/a$ space group (Fig. 2). Compositional dependence of the unit cell parameters for $Sr_{1-1.5x}Bi_xMoO_4$ compositions are shown in Fig. 2, where the linear chemical compression is caused by the substitution of the bigger cation with the smaller one (ionic radii $r_{Sr^{2+}}$ = 1.26 Å, $r_{Bi^{3+}}$ = 1.17 Å [17]). The measurements of density showed that experimental density is equal to the theoretical (X-ray) one to within the 2–3% of absolute values.

Synthesis of $Sr_{1-x}Bi_xMo_{1-x}V_xO_4$ results in the two-phase samples that consist of $BiVO_4$ (monoclinic) and $SrMoO_4$ phases. In contrast, $Ca_{1-x}Bi_xMo_{1-x}V_xO_4$ solid solutions are observed for $0 \le x \le 0.9$ [14]. One possible reason was that the dopants influence differently the composition and structure of strontium and calcium molybdates. The simultaneous presence of Bi and V in $Ca_{1-x}Bi_xMo_{1-x}V_xO_4$ leads to the expansion of the unit cell of a complex oxide due to the replacement of calcium with bismuth and compression of the unit cell due to the replacement of molybdenum with vanadium; as a result, the unit cell changes slightly [14] (ionic radii $r_{Ca^{2+}}$ = 1.12 Å, $r_{V^{5+}}$ = 0.54 Å, $r_{Mo^{6+}}$ = 0.41 Å [17]). In contrast, in $Sr_{1-x}Bi_xMo_{1-x}V_xO_4$ both of Bi and V lead to compression of the unit cell, making it unstable. It can be assumed that such compression of the unit cell leads to the decrease of the distance between $[BO_4]^{n-}$ (B = Mo, V) clusters and, consequently, to the increase of repulsion between them. As a result, the destruction of $Sr_{1-x}Bi_xMo_{1-x}V_xO_4$ system is observed. Creating an oxygen deficiency in the crystal lattice provides distortion in BO_4 tetrahedra and formation of $[BO_4]$–$[BO_3]^{n-}$-type bonds through common oxygen atoms. This can be realized by changing

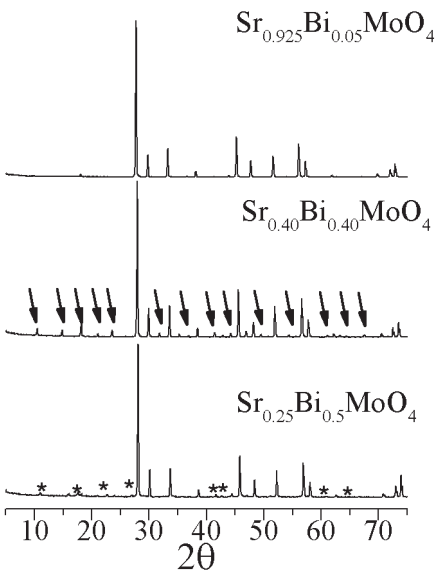

Fig. 1. X-ray diffraction profiles for selected $Sr_{1-1.5x}Bi_xMoO_4$ compositions. Arrows and asterisks indicate superlattice and $Bi_2Mo_3O_{12}$ reflections, respectively

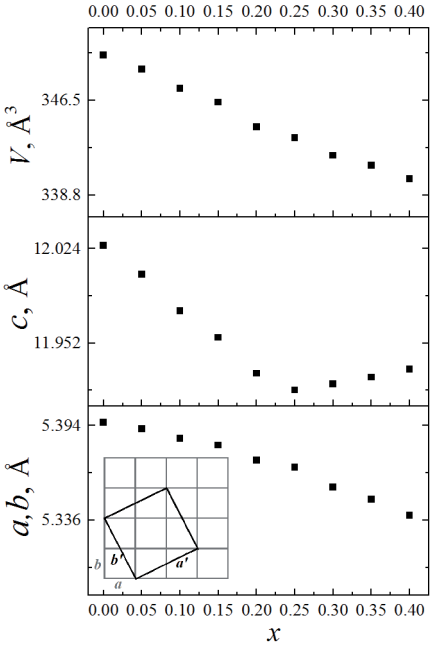

Fig. 2. Compositional variation of unit cell parameters in $Sr_{1-1.5x}Bi_xMoO_4$; super (*a*',*b*') and sub (*a*,*b*) — cells in $Sr_{1-1.5x}Bi_xMoO_4$ series (inset)

the composition of strontium molybdate to $Sr_{1-1.5x}Bi_xMo_{1-y}V_yO_{4-d}$.

It was expected that low concentration of bismuth would not provide a proper compression of the unit cell and single-phase samples would not be observed even at small *y*. But high concentration of bismuth can provide an efficient compression of the unit cell and the possibility of doping with vanadium. In fact, we observed such trend. For $x = 0.1$ in $Sr_{1-1.5x}Bi_xMo_{1-y}V_yO_{4-d}$ no single-phase samples was obtained, for $x = 0.2$ only $y = 0.05$ composition is single phase, for $x = 0.3$ and $x = 0.4$ single-phase compositions were observed at $y = 0.05–0.1$ and $0.05–0.2$, respectively. In this research, the maximum concentration of vanadium was not determined exactly, but the general trend is clear.

In the Table 1, the unit cell parameters of the single-phase samples are shown. When *x* is fixed and *y* increases or when *y* is fixed and *x* increases, a general compression of the unit cell is observed. The presence of vanadium in the structure leads to the absence of cationic ordering, and no additional peaks in X-ray diffraction profiles of $x = 0.3–0.4$ are observed. Unfortunately, it has proved impossible to accurately refine the oxide ion positions in the unit cell using a Rietveld approach, due to dominance of the X-ray scattering by the cations in this system and only neutron diffraction can refute or confirm the specified theory about the $[BO_4]–[BO_3]^{n-}$-type bond formation.

Powders of the $Sr_{1-1.5x}Bi_xMoO_4$ compositions were characterized by IR FT spectroscopy (Fig. 3). Several adsorption bands in the range of 950–500 cm^{-1} were detected. According to Basiev [18] sheelite-related compound ABO_4 consists of $[MoO_4]^{2-}$ clusters and isolated A^{2+} ions and, as a result, characteristic absorption bands can be assigned only to the vibrations in $[MoO_4]^{2-}$ clusters [19]. Strong absorption bands in the range 940–550 cm^{-1} are related to O–Mo–O stretches of the

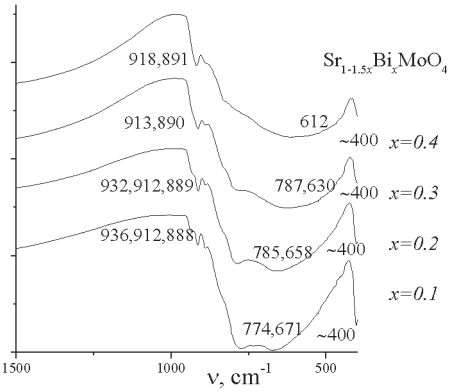

Fig. 3. IR FT spectra of the $Sr_{1-1.5x}Bi_xMoO_4$ compositions

Table 1

Unit cell parameters of $Sr_{1-1.5x}Bi_xMo_{1-y}V_yO_4$ ($0.1 < x < 0.4$, $0.05 < y < 0.2$) compositions

Composition	*a*, Å	*b*, Å	*c*, Å	*V*, Å^3
$Sr_{0.7}Bi_{0.2}Mo_{0.95}V_{0.05}O_4$	5.367	5.367	11.935	343.78
$Sr_{0.7}Bi_{0.2}Mo_{0.9}V_{0.1}O_4$	5.363	5.363	11.961	344.02
$Sr_{0.55}Bi_{0.3}Mo_{0.95}V_{0.05}O_4$	5.353	5.353	11.896	340.87
$Sr_{0.55}Bi_{0.3}Mo_{0.9}V_{0.1}O_4$	5.348	5.348	11.896	340.24
$Sr_{0.55}Bi_{03}Mo_{0.8}V_{0.2}O_4$	5.335	5.335	11.907	338.90
$Sr_{0.4}Bi_{0.4}Mo_{0.95}V_{0.05}O_4$	5.342	5.342	11.826	337.48
$Sr_{0.4}Bi_{0.4}Mo_{0.9}V_{0.1}O_4$	5.326	5.326	11.885	337.13
$Sr_{0.4}Bi_{0.4}Mo_{0.8}V_{0.2}O_4$	5.318	5.318	11.868	335.64

MoO_4 tetrahedron. Additional absorption band near 425–400 cm^{-1} can also be assigned to the deformational vibrations of O–Mo–O bands. In the IR FT spectra, the general shifting of absorption bands is observed. The same trend was observed for $Ca_{1-1.5x}Bi_xMoO_4$ [16]; in both cases it is caused by the deformation of MoO_4 tetrahedra resulting from the presence of cationic vacancies.

Conductivity measurements of $Sr_{1-1.5x}Bi_xMoO_4$ ceramic showed very high resistivity of samples (Fig. 4). A slight increase of conductivity is observed for the samples with superstructural ordering ($0.2 < x < 0.45$) and two-phase samples ($x > 0.45$).

Changing of dielectric loss tangent (tgδ) was measured at the range of 303–903 K at cooling at the fixed frequency of 1 kHz using the parallel R_p + C model (series connected R_s and Ls were shown to be negligible). The tgδ *vs* temperature curves of $Sr_{1-1.5x}Bi_xMoO_4$ compositions are shown at Fig. 5. The acceptable dielectric losses (tgδ < 0.1) of $Sr_{1-1.5x}Bi_xMoO_4$ compositions were observed for temperatures below ~573 K, while tgδ decreases with x values until $x = 0.3$. Then, at $x > 0.3$, tgδ increases, probably because of structural ordering of the samples.

For $Sr_{1-1.5x}Bi_xMo_{1-y}V_yO_{4-d}$ compositions we observed a significant growth in conductivity in comparison with $Sr_{1-1.5x}Bi_xMoO_4$. As a result, in the range of ~303–573 K the tgδ rises by approximately one order (Fig. 6). It is consistent with the increase of oxygen ion conductivity associated with structural changes.

The tgδ *vs* frequency dependences of all compositions of substituted $SrMoO_4$ indicate that effective dielectric properties are observed at frequency above 1 MHz, i.e. in the microwave range, as well

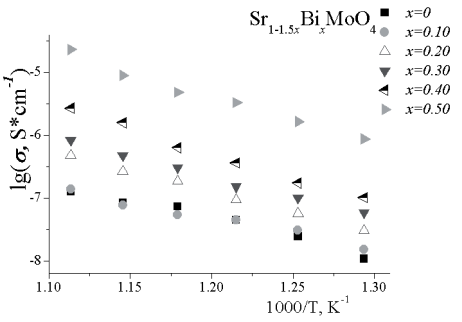

Fig. 4. Arrhenius plots for selected $Sr_{1-1.5x}Bi_xMoO_4$ compositions

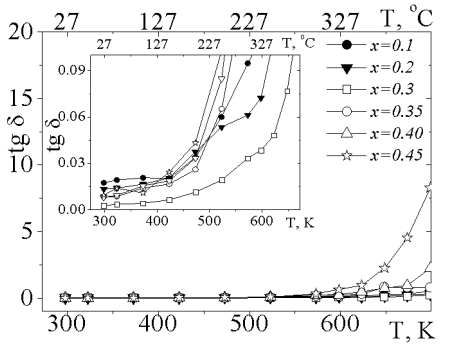

Fig. 5. The tgδ *vs* temperature curves of $Sr_{1-1.5x}Bi_xMoO_4$ compositions at 1 kHZ

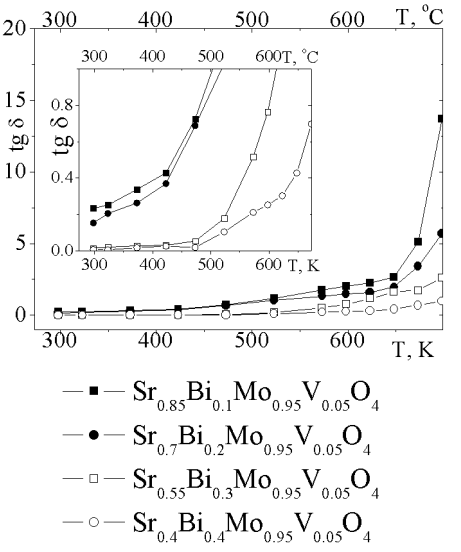

Fig. 6. The tgδ *vs* temperature curves of several $Sr_{1-1.5x}Bi_xMo_{1-y}V_yO_{4-d}$ compositions at 1 kHZ

as $CaMoO_4$ — based dielectric materials [16] (the example is given in Fig. 7).

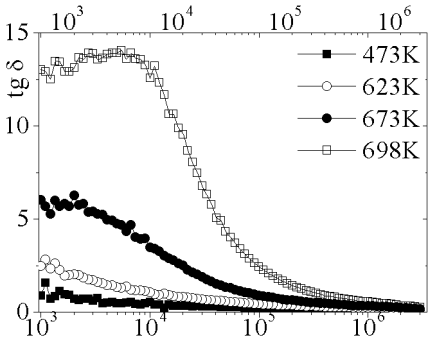

Fig. 7. The tgδ *vs* frequency curves of $Sr_{0.7}Bi_{0.2}Mo_{0.9}V_{0.1}O_{4-d}$

Conclusions

Thus, the present research demonstrates the existence of cationic-deficient sheelite-related complex oxides of $Sr_{1-1.5x}Bi_xMoO_4$ series and $Sr_{1-1.5x}Bi_xMo_{1-y}V_yO_{4-d}$ series. In $Sr_{1-1.5x}Bi_xMoO_4$, superstructural ordering is observed for $0.2 < x \leq 0.4$. For $Sr_{1-1.5x}Bi_xMo_{1-y}V_yO_{4-d}$ series a changing in oxygen sublattice is assumed. Both of the complex oxide series show dielectric properties at temperatures below 503 K and frequencies above 1 MHz. Conductivity and tangent of dielectric loss for $Sr_{1-1.5x}Bi_xMo_{1-y}V_yO_{4-d}$ compositions is greater than for $Sr_{1-1.5x}Bi_xMoO_4$. It is consistent with the increase of oxygen ion conductivity associated with mentioned structural changes.

Acknowledgements

This work was financially supported by grant of Russian Foundation for Basic Research, project № 16-33-60026.

References

1. Mikhailik VB, Kraus H, Miller G, Mykhaylyk MS, Wahl D. Luminescence of $CaWO_4$, $CaMoO_4$, and $ZnWO_4$ scintillating crystals under different excitations. J. Appl. Phys. 2005:97(8):083523. DOI: 10.1063/1.1872198.
2. Faure N, Borel C, Couchaud M, Basset G, Templier R, and Wyon C. Optical properties and laser performance of neodymium doped scheelites $CaWO_4$ and $NaGd(WO_4)_2$. Appl. Phys. B: Lasers Opt. 1996:63(6):593–98. DOI: 10.1007/BF01830998.
3. Sharma N, Shaju KM, Rao GVS, Chowdari BVR, Dong ZL, White TJ. Carbon-Coated Nanophase $CaMoO_4$ as Anode Material for Li Ion Batteries. Chem. Mater. 2004:16 (3):504–12. DOI: 10.1021/cm0348287.
4. Cavalcante LS, Longo VM, Sczancoski JC, Almeida MAP, Batista AA, Varela JA, Orlandi MO, Longo E, Liu MS. Electronic structure, growth mechanism and photoluminescence of $CaWO_4$ crystal. Cryst. Eng. Comm. 2012:14(3):853–68. DOI: 10.1039/C1CE05977G.
5. Yao WF, Ye JHJ. Photophysical and photocatalytic properties of $Ca_{1-x}Bi_xV_{x-}Mo_{1-x}O_4$ solid solutions. Phys. Chem. B. 2006:110(23):11188–95. http://dx.doi.org/10.1021/jp0608729.

6. Choi GK., Kim JR., Yoon SH., Hong KS. Microwave dielectric properties of scheelite (A = Ca, Sr, Ba) and wolframite (A = Mg, Zn, Mn) $AMoO_4$ compounds. J. Eur. Ceram. Soc. 2007:27(8-9):3063–67. DOI: 10.1016/j.jeurceramsoc.2006.11.037.
7. Esaka T, Mina-ai T, Iwahara H. Oxide ion conduction in the solid solution based on the scheelite-type oxide PbWO4 // Solid State Ionics: 1992:57(3-4): 319–25. DOI: 0.1016/0167–2738(92)90165-L
8. Zhang GG., Fang QF., Wang XP., Yi ZG. Dielectric relaxation study of $Pb_{1-x}La_xMoO_{4+\delta}$ (x = 0–0.3) oxide-ion conductors. J. Phys.: Condens. Matter. 2003:15(24): 4135–42. DOI: 10.1088/0953–8984/15/24/307.
9. Cheng J, Liu C, Cao W, Qi M, Shao G. Synthesis and electrical properties of scheelite $Ca_{1-x}Sm_xMoO_{4+d}$ solid electrolyte ceramics. Mat. Res. Bull. 2011:46(2):185–89. DOI: 10.1016/j.materresbull.2010.11.019.
10. Md. Haque M., Kim D-K. Luminescent properties of Eu activated $MLa_2(MoO_4)_4$ based (M=Ba, Sr and Ca) novel red-emitting phosphors. Mater. Lett. 2009:3(9-10):793–96. DOI: 10.1016/j.matlet.2009.01.018.
11. Jiang P., Gao W., Cong R., Yang T. Structural investigation of the A-site vacancy in scheelites and the luminescence behavior of two continuous solid solutions $A_{1-1.5x}Eu_x\square_{0.5x}WO_4$ and $A_{0.64-0.5y}Eu_{0.24}Li_y\square_{0.12-0.5y}WO_4$ (A = Ca, Sr; $\square$ = vacancy). Dalton Trans. 2015:44(13):6175–83. DOI: 10.1039/c5dt00022j.
12. Tomaszewicz E, Kaczmarek SM, Fuks H. New cadmium and rare-earth metal molybdates with scheelite type structure // Mater. Chem. Phys. 2010:122(2-3):595–601. DOI: 10.1016/j.matchemphys.2010.03.052.
13. Su Y, Li L, Li G. Synthesis and optimum luminescence of $CaWO_4$-based red phosphors with codoping of Eu^{3+} and Na^+. Chem. Mater. 2008:20(19):6060–67. DOI: 10.1021/cm8014435.
14. Sameera S, Prabhakar Rao P, Divya S, Raj KV, Aju Thara TR. High IR reflecting $BiVO_4$-$CaMoO_4$ based yellow pigments for cool roof applications. Energ. Buildings. 2017:154:491–98. DOI: 10.1016/j.enbuild.2017.08.089.
15. Sleight AW, Aykan K, Rogers DB. New nonstoichiometric molybdate, tungstate, and vanadate catalysts with the scheelite-type structure. J. Solid State Chem. 1975:13(3):231–36. DOI: 10.1016/0022–4596(75)90124–3.
16. Guo J, Randall CA, Zhang G, Zhou D, Chen Y, Wang H. Synthesis, structure, and characterization of new low-firing microwave dielectric ceramics: $Ca_{1-3x}Bi_{2x}\Phi_xMoO_4$. J. Mater. Chem. C. 2014:2(35):7364–72. DOI: 10.1039/c4tc00698d.
17. Shannon RD. Revised effective ionic radii and systematic studies of interatomic distances in halides and chalcogenides. Acta Cryst. 1976;A32:751–67. DOI: 10.1107/S0567739476001551.
18. Basiev TT, Sobol AA, Voronko YK, Zverev PG. Spontaneous Raman spectroscopy of tungstate and molybdate crystals for raman lasers. Opt. Mater.2000:15(3):205–16. DOI: 10.1016/S0925-3467(00)00037–9.
19. Cho Y, Bull Y. Fine-tuning the emission color of a transparent suspension of Sr-MoO_4: Eu^{3+},Tb^{3+} nanophosphors. Korean Chem. Soc. 2015:36(1):282–86. DOI: 10.1002/bkcs.10065.

Porotnikova N. M., Antonova E. P., Khodimchuk A. V.,
Tropin E. S., Farlenkov A. S., Ananyev M. V.
Chimica Techno Acta. 2018. Vol. 5, No. 4. P. 196–204.
ISSN 2409–5613

DOI: 10.15826/chimtech.2018.5.04.04

N. M. Porotnikova[ab*], E. P. Antonova[ab], A. V. Khodimchuk[ab], E. S. Tropin[ab], A. S. Farlenkov[ab], M. V. Ananyev[ab]

[a] Institute of High Temperature Electrochemistry, Ural Branch of Russian Academy of Sciences, 20 Akademicheskaya St., Ekaterinburg, 620137, Russian Federation
[b] Ural Federal University, 19 Mira St., Ekaterinburg, 620002, Russian Federation
**E-mail: n.porotnikova@mail.ru*

Oxygen diffusion and surface exchange kinetics for the mixed-conducting oxide $La_{0.6}Sr_{0.4}Co_{0.8}Fe_{0.2}O_{3-\delta}$

Studies of oxygen surface exchange kinetics for $La_{0.6}Sr_{0.4}Co_{0.8}Fe_{0.2}O_{3-\delta}$ oxide were performed using the technique of isotopic exchange of molecular oxygen with analysis of gas phase isotopic composition in a static circulation system at the temperatures of 600–800 °C in the oxygen pressure range of 0.27–2.13 kPa. The values of interphase exchange rate and oxygen diffusion coefficient were determined. The effective activation energies for oxygen exchange and diffusion processes as well as the exponents in the dependence of these values versus oxygen pressure in the double logarithmic coordinates were calculated. The process of oxygen dissociative adsorption at the surface of $La_{0.6}Sr_{0.4}Co_{0.8}Fe_{0.2}O_{3-\delta}$ oxide was found to be the rate-determining stage.

Keywords: oxygen isotope exchange; oxygen diffusion; lanthanum-strontium cobaltite-ferrite; rate-determining stage

Received: 14.11.2018. Accepted: 11.12.2018. Published: 31.12.2018.

Introduction

Over the last decades, complex oxides with the perovskite structure based on the lanthanum cobaltite attract much attention as potential cathode materials for solid oxide electrochemical devices [1–4]. Variation of cations concentration in these oxides results in the physical-chemical properties changes in the oxide-based materials [5, 6]. Complex oxides with a common formula $La_{1-x}Sr_xCo_{1-y}Fe_yO_{3-\delta}$ are among the most perspective cathode materials. A sufficient amount of information available in the literature has focused on the study of phase equilibria and physicochemical properties of oxides in this system [7–13]. In order to create the effectively operating cathodes based on lanthanum-strontium cobaltite-ferrites, it is vital to understand in detail the oxygen exchange and diffusion mechanisms in these materials.

The main purpose of the present work was to study oxygen diffusion and surface exchange kinetics in $La_{0.6}Sr_{0.4}Co_{0.8}Fe_{0.2}O_{3-\delta}$ oxide.

Experimental

The $La_{0.6}Sr_{0.4}Co_{0.8}Fe_{0.2}O_{3-\delta}$ oxide was prepared using the citrate-nitrate technology. Lanthanum oxide (LaO-D, 99,99635%), strontium carbonate $SrCO_3$ (ACS), cobalt nitrate $Co(NO_3)_2 \cdot 6H_2O$ (chemically pure), iron citrate $C_6H_5FeO_7 \cdot H_2O$ (Fluka Analytical) were used as initial reagents. The synthesis was performed at the temperature of 1100 °C for 5 hours.

In order to perform the oxygen isotope exchange measurements, dense ceramic was fabricated. The obtained powders were ground and compacted into the form of disks using 1% water solution of polyvinyl alcohol that served as a bounding agent. The final sintering was performed at the temperature of 1250 °C for 5 hours in air. A relative density of the obtained ceramics was about ~ 92%. Finally, the sintered dense specimens were polished using diamond pastes, such as ACM 7/5 NVMC (Federal Standard 25593–83) and ACM 1/0 NOM (Federal Standard 16377–71).

The phase composition of the $La_{0.6}Sr_{0.4}Co_{0.8}Fe_{0.2}O_{3-\delta}$ sample was determined before and after the isotope experiments using a Rigaku D/MAX-2200V diffractometer in the Cu Ka emission at room temperature. According to the X-ray analysis, the sample was single phase after synthesis ($R\bar{3}c$ space group, cell parameters a = 5.4270(4) Å, c = 13.239(2) Å) and after completing measurements at high temperatures and low oxygen pressures (Fig. 1), which confirms its stability during long-term tests.

The analysis of the particle size distribution for powder materials was performed by the laser scattering method using a Malvern Mastersizer 2000. To grind the agglomerated particles, the slurry was mixed using a stirrer with the rate of ~2000 rpm, as well as subjected to an ultrasound treatment. Fig. 2 illustrates the volume fraction versus particle size distribution function.

The microphotographs of the ceramics cross-section were made by a scanning electron microscope Tescan MIRA 3. Fig. 3 presents the microphotograph obtained in a beam of back-scattered electrons. The contrast of the images is mainly due to the chemical composition of the studied material surface. As can be seen from Fig. 4, there are small inclusions of cobalt-rich phase at the grains boundaries (probably cobalt oxide); however, the fraction is insignificant, it is less than 0.5%.

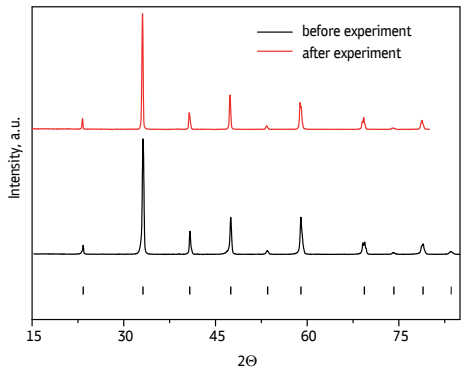

Fig. 1. XRD patterns for $La_{0.6}Sr_{0.4}Co_{0.8}Fe_{0.2}O_{3-\delta}$ oxide before and after isotope experiments

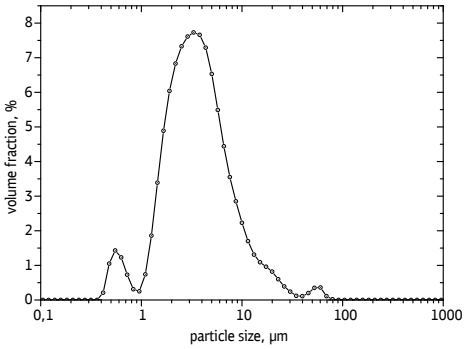

Fig. 2. Particle size distribution function for the $La_{0.6}Sr_{0.4}Co_{0.8}Fe_{0.2}O_{3-\delta}$ powder

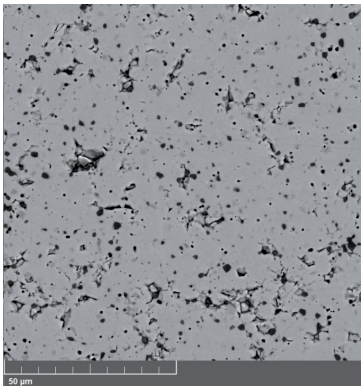

Fig. 3. SEM image of cross-section of $La_{0.6}Sr_{0.4}Co_{0.8}Fe_{0.2}O_{3-\delta}$ ceramics in BSE mode

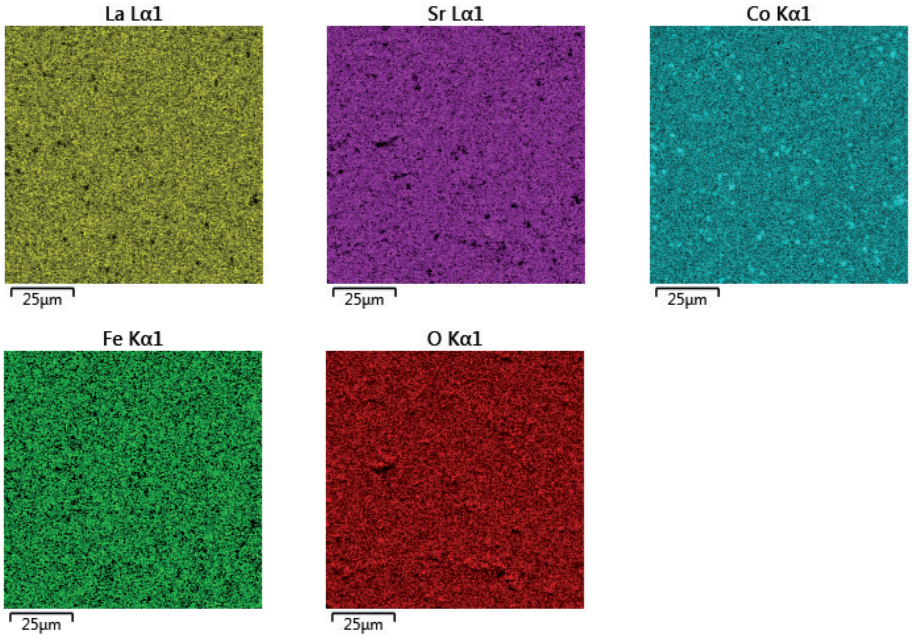

Fig. 4. EDX mapping for $La_{0.6}Sr_{0.4}Co_{0.8}Fe_{0.2}O_{3-\delta}$ ceramics

The oxygen exchange kinetics between the gas phase and oxide was studied by the oxygen isotope exchange method with gas phase equilibration in the experimental rig [12]. Enriched oxygen ^{18}O, whose fraction was 83.6%, served as a match mark. During the experiment, the changes in concentrations of three mass numbers — C_{32}, C_{34}, C_{36} — were recorded depending on time using a quadrupolar mass-spectrometer Agilent 5973N. The detailed description of the experiment methodology, evaluation of the interphase exchange rate detection accuracy (r_H, atom·cm^{-2} · s^{-1}) and oxygen diffusion coefficient (D, cm^2·s^{-1}) has been reported elsewhere [14, 15]. The oxygen interphase exchange rate is numerically equal to the number of oxygen atoms, which exchange at the surface of a unit area per unit of time. The isotope exchange method is one of the few direct methods of oxygen exchange kinetics study, which advantage is a possibility to obtain information

on the oxygen redistribution between a solid oxide and gaseous phase in the adsorption-desorption equilibrium. This allows obtaining high accuracy for the kinetics characteristic values. To compare the obtained values of the interphase exchange rate with the literature data the following translation formula was used:

$$k = r_H \frac{M_r}{(3-\delta)N_A \rho}, \quad (1)$$

where r_H is the oxygen interphase exchange rate (atom·cm^{-2} · s^{-1}), k is the oxygen exchange coefficient (cm · s^{-1}), M_r is the molecular mass, δ is the oxygen non-stoichiometry, N_A is the Avogadro constant, ρ is the sample crystallographic density.

Results and discussion

The oxygen exchange kinetics for the $La_{0.6}Sr_{0.4}Co_{0.8}Fe_{0.2}O_{3-\delta}$ oxide was studied at the temperatures of 600–800 °C and the oxygen pressure interval 0.27–2.13 kPa. During the experiment, the changes in ionic current, which correspond to the weight of 32, 34 and 36, versus the exchange time were recorded. Then the obtained values were recalculated into the mass numbers concentrations (see Fig. 5). Typical time dependence for the ^{18}O oxygen isotope fraction changes in a particular experimental condition is presented in Fig. 6. The obtained data can be described using the model developed by Ezin et al. [16] on the basis of the solution suggested by Klier et al. [17].

Fig. 7 illustrates the dependencies of the interphase exchange rate versus oxygen pressure in logarithmic coordinates at different temperatures for the $La_{0.6}Sr_{0.4}Co_{0.8}Fe_{0.2}O_{3-\delta}$ oxide. The values of exchange rate increase noticeably as the oxygen pressure and temperature rise. The dependence of interphase exchange rate versus oxygen pressure exhibited a form of the exponential function: $r_H \sim P_{O_2}^n$. The exponent values that were calculated from the line slopes decreased from 1.03 ± 0.04 down to 0.52 ± 0.03 as the temperature rose.

Boreskov et al. [18] proved that the oxygen exchange occurs at the elevated temperatures according to the oxygen dissociative adsorption-desorption mechanism for a number of simple oxide systems. In particular, the oxides with equilibrium

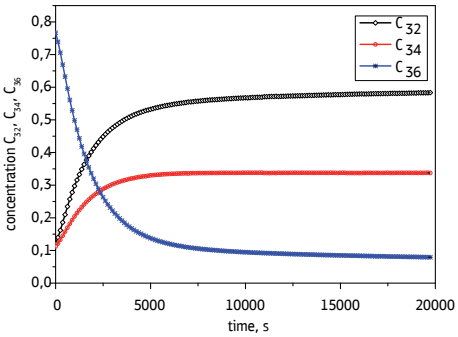

Fig. 5. Experimental concentrations of C_{32}, C_{34}, C_{36} in the gas phase versus time (T = 800 °C, P_{O2} = 0.53 kPa)

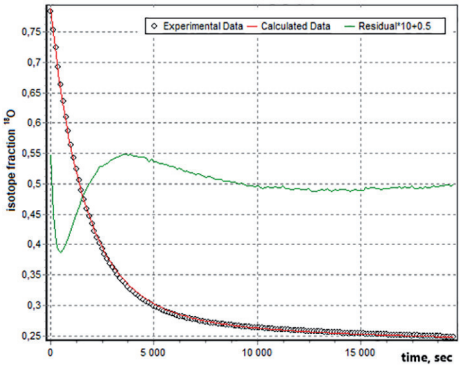

Fig. 6. Fraction of ^{18}O-isotope in the gas phase vs. time in the typical isotope exchange experiment at T = 800 °C, P_{O2} = 0.53 kPa. Points are experimental data, and the line is the fitting result

oxygen concentration do not obey the first type of the exchange mechanism, according to which oxygen atom from the surface does not involved. The isotope exchange proceeds mainly according to the second and third exchange types with the participation of one or two oxygen atoms from the surface. Recently, for the complex oxide systems [15, 19–23] we have demonstrated that the exponents in the equations for the oxygen interphase exchange versus oxygen pressure varies depending on the process which is a rate-determining stage. Often the exchange at high temperature occurs according to the oxygen dissociative adsorption mechanism. Depending on the relation of three exchange types contribution, the oxygen exchange mechanism differs for oxides.

Fig. 8 demonstrates the dependence of the tracer diffusion coefficients of oxygen versus oxygen pressure at various temperatures. The value of the oxygen diffusion coefficient is almost independent of oxygen pressure. Earlier [15] we demonstrated the influence of the oxygen nonstoichiometry on the value of the oxygen tracer diffusion coefficient, for example in lanthanum strontium cobaltites. Almost constant value of oxygen tracer diffusion coefficient in the Fe-doped lanthanum strontium cobaltite is likely associated with the insignificant changes in the oxygen vacancies concentration within the oxygen pressures range of $0.27 \le Po_2 \le 2.13$ kPa, which was also confirmed earlier [24–26].

Figs. 9, 10 illustrate the temperature dependencies of oxygen exchange coefficient and oxygen diffusion coefficient, respectively, in comparison with literary data for different oxides [22, 26–29]. The values of activation energy for the exchange and diffusion processes are listed in Table 1. It should be noted that relatively high values of oxygen diffusion and exchange coefficients for the studied $La_{0.6}Sr_{0.4}Co_{0.8}Fe_{0.2}O_{3-\delta}$ oxide are comparable with the values for barium praseodymium cobaltite [29] and are greater by the value of magnitude than those for lanthanum strontium manganite [22]. Therefore, it may be assumed that $La_{0.6}Sr_{0.4}Co_{0.8}Fe_{0.2}O_{3-\delta}$ is a perspective oxide for the SOFC cathode materials, because of its high values of exponents in the equation for oxygen exchange reaction and good stability in the reducing atmosphere. The substitution of iron for cobalt results in the insignifi-

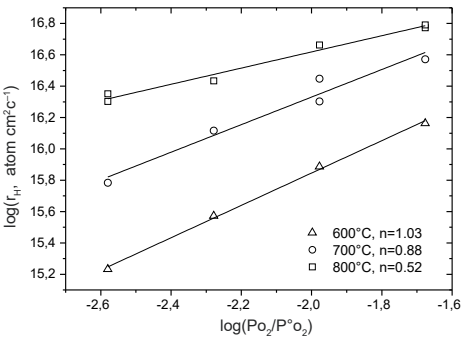

Fig. 7. The oxygen interphase exchange for $La_{0.6}Sr_{0.4}Co_{0.8}Fe_{0.2}O_{3-\delta}$ plotted as a function of oxygen partial pressure at different temperatures, $P^{o}o_2 = 101.3$ kPa (n ~ *tg*β)

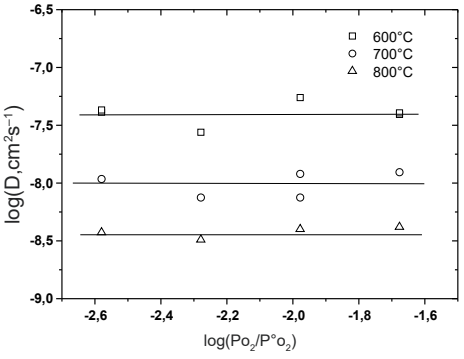

Fig. 8. Oxygen diffusion coefficients versus oxygen partial pressure at different temperatures for the $La_{0.6}Sr_{0.4}Co_{0.8}Fe_{0.2}O_{3-\delta}$ oxide

Table 1

The apparent activation energy values for the oxygen surface exchange and oxygen diffusion processes in the mixed conducting oxides

Oxide	Oxygen pressure, kPa	ΔT, °C	Activation energy, eV		Source
			Exchange	Diffusion	
$La_{0.6}Sr_{0.4}Co_{0.8}Fe_{0.2}O_{3-\delta}$	2.13	600–800	0.57 ± 0.05	0.92 ± 0.05	This work
$La_{0.6}Sr_{0.4}CoO_{3\pm\delta}$	0.67	600–850	0.11	1.08	[26]
$La_{0.6}Sr_{0.4}MnO_{3\pm\delta}$	0.67	700–850	0.71	1.42	[22]
$Pr_2NiO_{4\pm\delta}$	0.67	600–700 700–800	2.0 1.4	2.0	[27]
$La_2NiO_{4\pm\delta}$	1.33	600–800	1.38	1.41	[28]
$PrBaCo_2O_{6-\delta}$	1.33	600–800	0.76	0.75	[29]

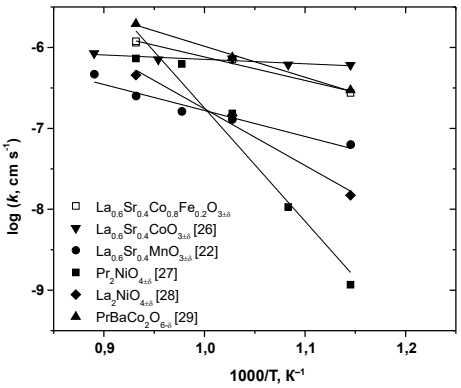

Fig. 9. Temperature dependences of the oxygen exchange coefficient for various mixed conducting oxides

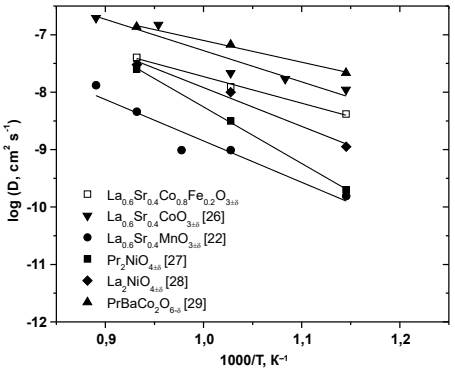

Fig. 10. Temperature dependences of the oxygen tracer diffusion coefficient for various mixed conducting oxides

cant decrease in the oxygen exchange rate; however, its introduction into the cobalt sublattice increases the stability of oxide in the reducing atmospheres [6].

Conclusions

The oxygen exchange kinetics for the $La_{0.6}Sr_{0.4}Co_{0.8}Fe_{0.2}O_{3-\delta}$ oxide was studied using the isotope exchange method with gas phase equilibration. The values of the interphase exchange rate and oxygen diffusion coefficient in $La_{0.6}Sr_{0.4}Co_{0.8}Fe_{0.2}O_{3-\delta}$ were calculated. The values of effective activation energies for the oxygen interphase exchange and diffusion were calculated.

The exponents in the equations for the oxygen interphase exchange rate were found within the range of 0.52–1.03 at the temperatures of 600–800 °C in the oxygen pressures range of 0.27–2.13 kPa.

Based on these results, it can be concluded that the exchange in the case of $La_{0.6}Sr_{0.4}Co_{0.8}Fe_{0.2}O_{3-\delta}$ occurs according to the mechanism of the molecular oxygen dissociative adsorption at the oxide surface.

The obtained results demonstrate that $La_{0.6}Sr_{0.4}Co_{0.8}Fe_{0.2}O_{3-\delta}$ possesses high values of oxygen interphase exchange rate and oxygen diffusion coefficient as compared to other oxide materials with mixed conductivity.

Acknowledgements

This work is partly supported by the Russian Science Foundation (Project No. 17-73-10196) using facilities of shared access center "Composition of Compounds" of IHTE UB RAS.

References

1. Petrov AN, Cherepanov VA, Zuyev AYu, Zhukovsky VM. Thermodynamic stability of ternary oxides in Ln–M–O systems (Ln = La, Pr, Nd; M = Co, Ni, Cu). *J Solid State Chem.* 1988;77(1):1–14. DOI: 10.1016/0022–4596(88)90083–7.
2. Kharton VV, Figueiredo FM, Kovalevsky AV, Viskup AP, Naumovich EN, Yaremchenko AA, Bashmakov IA, Marques FM. Processing, microstructure and properties of $LaCoO_{3-\delta}$ ceramics. *J Eur Ceram Soc.* 2001;21(13):2301–9. DOI: 10.1016/S0955-2219(01)00199–6.
3. Yang M, Zhong Y, Liu ZK. Defect analysis and thermodynamic modeling of $LaCoO_3$. *Solid State Ionics.* 2007;178(15-18):1027–32. DOI: 10.1016/j.ssi.2007.04.014.
4. Zuev AYu, Petrov AN, Vylkov AI, Tsvetkov DS. Oxygen nonstoichiometry and defect structure of undoped and doped lanthanum cobaltites. *Journal of Material Sciences.* 2007;42(6):1901–8. DOI: 10.1007/s10853-006-0345-8.
5. Tai LW, Nasrallah MM, Anderson HU, Sparlin DM, Sehlin SR. Structure and electrical properties of $La_{1-x}Sr_xCo_{1-y}Fe_yO_3$. Part 1. The system $La_{0.8}Sr_{0.2}Co_{1-y}Fe_yO_3$ // *Solid State Ionics.* 1995;76(3-4):259–71. DOI: 10.1016/0167–2738(94)00244-M.
6. Stevenson JW, Armstrong TR, Carneim RD, Pederson LR, Weber WJ. Electrochemical properties of mixed conducting perovskites $La_{1-x}M_xCo_{1-y}Fe_yO_{3-\delta}$ (M = Sr, Ba, Ca). *J Electrochem Soc.* 1996;143(9) 2722–9. DOI: 10.1149/1.1837098.
7. Aksenova TV, Anan'ev MV, Gavrilova LYa, Cherepanov VA. Phase equilibria and crystal structures of solid solutions in the system $LaCoO_{3-\delta}$–$SrCoO_{2.5\pm\delta}$–$SrFeO_{3-\delta}$–$LaFeO_{3-\delta}$. *Inorg Mater.* 2007;43(3):296–300. DOI: 10.1134/S0020168507030168.
8. Lankhorst MHR, Elshof JE. Thermodynamic quantities and defect structure of $La_{0.6}Sr_{0.4}Co_{1-y}Fe_yO_{3-\delta}$ (y=0–0.6) from high-temperature coulometric titration experiments. *J Solid State Chem.* 1997;130(2):302–10. DOI: 10.1006/jssc.1997.7378.
9. Choi MB, Lim DK, Wachsman ED, Song SJ. Oxygen nonstoichiometry and chemical expansion of mixed conducting $La_{0.1}Sr_{0.9}Co_{0.8}Fe_{0.2}O_{3-\delta}$. *Solid State Ionics.* 2012;221:22–7. DOI: 10.1016/j.ssi.2012.06.012.
10. Hashimoto S, Fukuda Y, Kuhn M, Sato K, Yashiro K, Mizusaki J. Oxygen nonstoichiometry and thermo-chemical stability of $La_{0.6}Sr_{0.4}Co_{1-y}Fe_yO_{3-\delta}$ (y=0.2, 0.4, 0.6, 0.8). *Solid State Ionics.* 2010;181(37-38):1713–9. DOI: 10.1016/j.ssi.2010.09.024.

11. Elshof JE, Lankhorst MHR, Bouwmeester HJM. Chemical diffusion and oxygen exchange of $La_{0.6}Sr_{0.4}Co_{0.6}Fe_{0.4}O_{3-\delta}$. *Solid State Ionics.* 1997;99(1-2):15–22. DOI: 10.1016/S0167-2738(97)00263–4.
12. Ananyev MV, Kurumchin EKh. Interphase exchange and diffusion of oxygen in lanthanum-strontium cobaltites doped with iron. *Russ J Phys Chem A.* 2010;84(6):1039–44. DOI: 10.1134/S0036024410060269.
13. Bouwmeester HJM, den Otter MW, Boukamp BA. Oxygen transport in $La_{0.6}Sr_{0.4}Co_{1-y}Fe_yO_{3-\delta}$. *J Solid State Electrochem.* 2004;8(9):599–605. DOI: 10.1007/s10008-003-0488-3.
14. Kurumchin EKh, Ananjev MV, Vdovin GK, Surkova MG. Exchange kinetics and diffusion of oxygen in systems based on lanthanum gallate. *Russ J Electrochem.* 2010;46(2):205–11. DOI: 10.1134/S1023193510020126.
15. Ananyev MV, Kurumchin EKh, Porotnikova NM. Effect of oxygen nonstoichiometry on kinetics of oxygen exchange and diffusion in lanthanum-strontium cobaltites. *Russ J Electrochem.* 2010;46(7):789–97. DOI: 10.1134/S1023193510070128.
16. Ezin AN, Tsidilkovski VI, Kurumchin EKh. Isotopic exchange and diffusion of oxygen in oxides with different bulk and subsurface diffusivities. *Solid State Ionics.* 1996;84(1-2):105–12. DOI: 10.1016/S0167-2738(96)83012–8.
17. Klier K, Kucera E. Theory of Exchange Reactions between Fluids and Solids with Tracer Diffusion in the Solid. *J Phys Chem Solids.* 1966;27:1087–95. DOI: 10.1016/0022–3697(66)90084–9.
18. Boreskov GK, Kasatkina LA. Catalysis of Isotope Exchange in Molecular Oxygen and Its Application to the Study of Catalysts. *Russ Chem Rev.* 1968;37(8):613–28. DOI: 10.1070/RC1968v037n08ABEH001686.
19. Porotnikova NM, Anan'ev MV, Kurumchin EKh. Effect of Defect Structure of Lanthanum Manganite on Kinetics of Oxygen Exchange and Diffusion. *Russ J Electrochem.* 2011;47(11):1250–6. DOI: 10.1134/S1023193511110139.
20. Anan'ev MV, Bershitskaya NM, Plaksin SV, Kurumchin EKh. Phase equilibriums, oxygen exchange kinetics and diffusion in oxides $CaZr_{1-x}Sc_xO_{3-x/2-\delta}$. *Russ J Electrochem.* 2012;48(9):879–86. DOI: 10.1134/S1023193512090030.
21. Anan'ev MV, Kurumchin EKh, Vdovin GK, Bershitskaya NM. Kinetics of interaction of gas phase oxygen with cerium-gadolinium oxide. *Russ J Electrochem.* 2012;48(9):871–8. DOI: 10.1134/S1023193512090029.
22. Bershitskaya NM, Ananyev MV, Kurumchin EKh, Gavrilyuk AL, Pankratov AA. Effect of oxygen nonstoichiometry on kinetics of oxygen exchange and diffusion in lanthanum-strontium manganites. *Russ J Electrochem.* 2013;49(10):963–74. DOI: 10.1134/S1023193512100047.
23. Wang S, Katsuki M, Dokiya M, Hashimoto T. High temperature properties of $La_{0.6}Sr_{0.4}Co_{0.8}Fe_{0.2}O_{3-\delta}$ phase structure and electrical conductivity. *Solid State Ionics.* 2003;159(1-2):71–8. DOI: 10.1016/S0167-2738(03)00027–4.
24. Li Y, Gerdes K, Horita T, Liu X. Surface exchange and bulk diffusivity of LSCF as SOFC cathode: electrical conductivity relaxation and isotope exchange characterizations. *J Electrochem Soc.* 2013;160(4):F343–50. DOI: 10.1149/2.044304jes.

25. Katsuki M, Wang S, Dokiya M, Hashimoto T. High temperature properties of $La_{0.6}Sr_{0.4}Co_{0.8}Fe_{0.2}O_{3-\delta}$ oxygen nonstoichiometry and chemical diffusion constant. *Solid State Ionics*. 2003;156(3-4):453–61. DOI: 10.1016/S0167-2738(02)00733–6.
26. Ananyev MV. Izotopnii obmen kisloroda. Teoreticheskie osnovy metoda i ego primenenie k analizy kinetiki obmena kisloroda s stehiometricheskimi oksidami [Oxygen isotope exchange. Theoretical basis of the method and its application to the analysis of the kinetics of oxygen exchange with non-stoichiometric oxides] Saarbrucken: Lambert Academic Publishing; 2012. 205 p. Russian.
27. Porotnikova NM, Khodimchuk AV, Ananyev MV, Eremin VA, Tropin ES, Farlenkov AS, Pikalova EYu, Fetisov AV. *J Solid State Electrochem.* 2018;22(7):2115–26. DOI: 10.1007/s10008-018-3919-x.
28. Ananyev MV, Tropin ES, Eremin VA, Farlenkov AS, Smirnov AS, Kolchugin AA, Porotnikova NM, Khodimchuk AV, Berenov AV, Kurumchin EK. Oxygen isotope exchange in $La_2NiO_{4\pm\delta}$. *Phys Chem Chem Phys.* 2016;18(13):9102–11. DOI: 10.1039/c5cp05984d.
29. Ananyev MV, Eremin VA, Tsvetkov DS, Porotnikova NM, Farlenkov AS, Zuev AYu, Fetisov AV, Kurumchin EKh. Oxygen isotope exchange and diffusion in $LnBaCo_2O_{6-\delta}$ (Ln = Pr, Sm, Gd) with double perovskite structure. *Solid State Ionics*. 2017;304:96–106. DOI: 10.1016/j.ssi.2017.03.022.

Samigullina R. F., Rotermel M. V., Ivanova I. V., Krasnenko T. I.
Chimica Techno Acta. 2018. Vol. 5, No. 4. P. 205–209.
ISSN 2409–5613

DOI: 10.15826/chimtech.2018.5.4.05

R. F. Samigullina, M. V. Rotermel*, I. V. Ivanova, T. I. Krasnenko

Institute of Solid State Chemistry,
Ural Branch of the Russian Academy of Sciences,
91 Pervomaiskaya St., Ekaterinburg 620990, Russian Federation
**E-mail: rotermel@ihim.uran.ru*

Sol-gel synthesis and crystal chemical properties of the pigment $Zn_{1.9}Cu_{0.1}SiO_4$

The pigment $Zn_{1.9}Cu_{0.1}SiO_4$ was obtained by the method of sol-gel synthesis. The crystallization temperature was set at 776 °C, $\Delta H \approx -16.3$ kJ/mol. Thermal expansion of the individual Zn_2SiO_4 and $Zn_{1.9}Cu_{0.1}SiO_4$ solid solutions was studied by in situ high-temperature X-ray diffraction. It is shown that the substitution of $Zn^{2+} \rightarrow Cu^{2+}$ does not lead to significant changes in the lattice parameters; in the range from room temperature to 800 °C the structure expands monotonically when heated. The coefficients of volumetric thermal expansion for Zn_2SiO_4 and $Zn_{1.9}Cu_{0.1}SiO_4$ are $\alpha_V = 8.05 \cdot 10^{-6}$ and $8.81 \cdot 10^{-6}$ 1/K, respectively. The colorimetric coordinates in the RGB system are 71.8% red, 72.9% green and 79.6% blue, which corresponds to the gray-blue pigment.

Keywords: pigment; willemite; sol-gel synthesis; thermal expansion.

Received: 06.12.2018. Accepted: 21.12.2018. Published: 31.12.2018.

Introduction

Divalent metal silicates are widely used as luminescent, corrosion protecting, electrical insulating materials, catalysts, pigments. Thus, the emergence of the chemical manufacturing of synthetic pigments began with the production of dyed double silicates, known as egyptian blue $CaCuSi_4O_{10}$, han blue $BaCuSi_4O_{10}$ [1–3]. The continued interest to the silicate pigments is caused due to the pure intense color, as well as by their high thermal and chemical resistance. Therefore, it is possible to use them for dyeing ceramic products that exposed to high temperature calcination in the manufacturing process. Transition metal orthosilicates containing copper, nickel, and cobalt ions are well known as blue pigments. Dopant M^{2+} ions (M = Cu, Ni, Co) in $Zn_{2-2x}M_{2x}SiO_4$ solid solutions are coordinated by four oxygen atoms, which causes the blue color of the compounds due to the splitting of electron levels of M^{2+} ions in the crystal field. Since the information about $Zn_{2-2x}M_{2x}SiO_4$ (M = Cu, Ni, Co) is limited, the purpose of this work is a disclosure of sol-gel synthesis mechanism for $Zn_{1.9}Cu_{0.1}SiO_4$ and determination of main pigment characteristics, such as colorimetric parameters and thermal expansion coefficient.

Experimental

The precursors used in the sol-gel synthesis of $Zn_{1.9}Cu_{0.1}SiO_4$ were zinc acetate $Zn(CH_3COO)_2{\cdot}2H_2O$, copper acetate $Cu(CH_3COO)_2{\cdot}H_2O$, and tetraethyl orthosilicate (TEOS) $Si(OC_2H_5)_4$. The phase composition within the range from room temperature up to 800 °C was controlled in situ by the X-ray powder diffraction (XRPD) method (Shimadzu diffractometer, $CuKa_1$ radiation, 2θ angle interval from 10 to 60° with a step of 0.02°), comparing the XRD data with the X-ray characteristics of the possible impurity oxides and zinc silicates (PDF2 database, ICDD, USA, Release 2009). The temperature was controlled using an Anton Paar TTK-450 attachment. The unit cell parameters were refined by the Rietveld method using the Fullprof 2010 software. Thermogravimetric (TG) analysis together with differential thermal analysis (DTA) were performed using a Setsys Evolution thermal analyzer (Setaram) in air at a temperature scan rate of 10 °/min in the temperature range 20–1100 °C, with alumina as a reference substance. Colorimetric analysis was performed using an SLR Olympus e-420 (light source temperature of 5400 K; ISO = 200; light camera parameters L×W×H = 35×25×32 cm) Photo Impact 12 program, through a calibrator monitor One-Eye Pro. The colorimetry results are given in the RGB color coordinates system.

Results and discussion

The synthesis method used in our work allowed us to obtain the Cu^{2+} dopant concentration equal to 5 at.%. Hydrolysis of $[Si(C_2H_5O)_4]$ in the mixture with the ratio H_2O:TEOS = 1:1 took place within 30 min. The alcohol solutions of metal acetates and hydrolized TEOS were mixed. After the solutions were poured together the mixture was stirred on a magnetic stirrer for 1 h. The precursor for the final stage of synthesis was obtained by evaporation of the mixture for 2 hours at 65 °C. The gel was formed after 2 days at room temperature.

In order to determine the temperature range of $Zn_{1.9}Cu_{0.1}SiO_4$ formation, thermogravimetric and differential thermal analyses of the obtained precursor were carried out (Fig. 1).

The mass loss of 2–3%, accompanied by a small endothermic effect at 100 °C, corresponds to the removal of water and ethanol residual. The weight loss of about 20% with a simultaneous exothermic signal on the DTA curve within the region of 250–410 °C is caused by the decomposition of organic components. The DTA curve shows the sharp exothermic effect ($\Delta H \approx -16.3$ kJ/mol) with a maximum at 776 °C, while the mass of the sample remains constant. The assignment of this effect was determined by the thermal analysis of Zn_2SiO_4 precursor, prepared from zinc acetate and TEOS (Fig. 2). The exothermic effect recorded on the DTA curve in the temperature range 320–500 °C with simultaneous mass loss on the TG curve corresponded to the decomposition of organic components. The exothermic effect at 786 °C ($\Delta H \approx -15.5$ kJ/mol) with a constant sample mass is similar to that observed on the DTA curve for the precursor with the nominal composition $Zn_{1.9}Cu_{0.1}SiO_4$ (Fig. 1). Consequently, one can conclude that the exothermal effects on the compared DTA curves for the Zn_2SiO_4 and $Zn_{1.9}Cu_{0.1}SiO_4$ precursors are of the same nature, and both are related

to the process of a phase with the willemite structure formation. Thus, a comparative analysis of the thermal behavior of these samples showed that at temperatures above 776 °C the process of forming a long-range order at sol-gel synthesis of $Zn_{1.9}Cu_{0.1}SiO_4$ was completed.

XRD data of the $Zn_{1.9}Cu_{0.1}SiO_4$ precursor annealed at 800 °C does indicate the formation of the phase with the willemite structure; however, an insignificant admixture of copper (II) oxide is present in the sample (Fig. 3). The single-phase product was obtained by firing the precursor sample at 900 °C (Fig. 3).

X-ray pattern of the single phase $Zn_{1.9}Cu_{0.1}SiO_4$ sample taken at room temperature was indexed in the willemite type structure with the trigonal space group $R\bar{3}$. The refined unit cell parameters, unit cell volume and number of formula units are: a = 13.927(1) Å, c = 9.305(3) Å, V = 1563.03(8) Å^3, Z = 18.

One of the most important characteristics of the pigment is the volumetric thermal expansion coefficient (VTEC), which should be comparable to the thermal expansion of the coated material. Colored zinc orthosilicate doped with copper may be suitable as a pigment for ceramics made of porcelain, earthenware, majolica. Manufacturing and operation proceeds in wide temperature range, therefore, the coincidence VTEC of the matrix and the pigment will allow to avoid cracking of the coating.

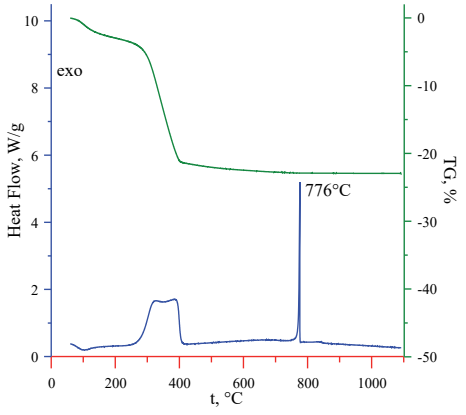

Fig. 1. TG and DTA curves (on heating) of the $Z_{1.9}Cu_{0.1}SiO_4$ precursor

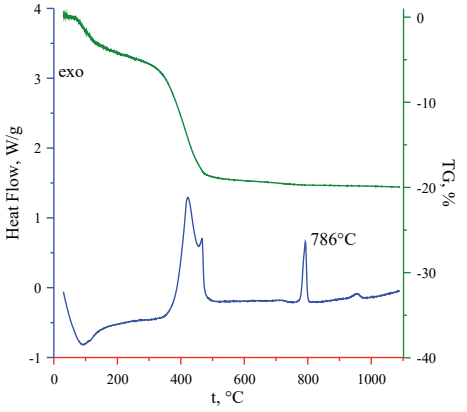

Fig. 2. Heating TG and DTA curves of the Zn_2SiO_4 precursor

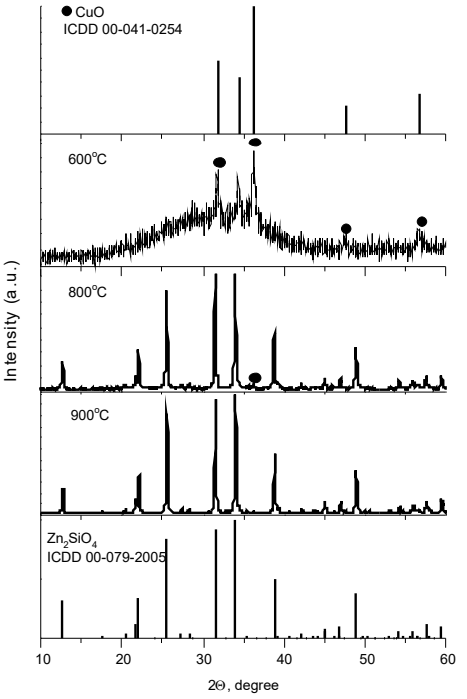

Fig. 3. X-ray diffraction profiles of $Zn_{1.9}Cu_{0.1}SiO_4$ powder annealed at different temperatures

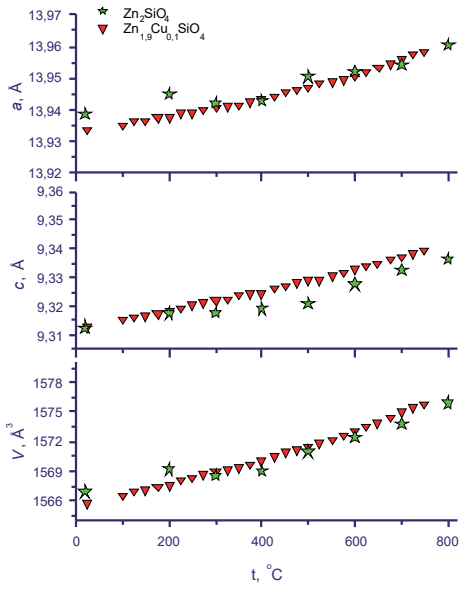

Fig. 4. The unit cell parameters and unit cell volume for $Zn_{2-2x}Cu_{2x}SiO_4$ (x = 0, 0.05) versus temperature

The values of VTEC were calculated from the experimental results for the $Zn_{2-2x}Cu_{2x}SiO_4$ unit cell parameters (x = 0; 0.05) in the range from room temperature up to 800 °C (Fig. 4). It was shown that the sizes of the unit cell for the zinc orthosilicate Zn_2SiO_4 and $Zn_{1.9}Cu_{0.1}SiO_4$ solid solution monotonically expanded with increasing temperature. Doping of zinc orthosilicate with the cations with similar size, like Cu^{2+} (for c.n.= 4 $r_{Zn^{2+}}$ = 0.74 Å, $r_{Cu^{2+}}$ = 0.71 Å) does not lead to significant differences in the polyterms of unit cell parameters. A comparison of VTEC for $Zn_{2-2x}Cu_{2x}SiO_4$ (x = 0; 0.05) with that for the ceramic substrate [4], most often used as a coated material (Table 1), shows their proximity.

Table 1

Volume thermal expansion coefficients for the often used ceramics and $Zn_{2-2x}Cu_{2x}SiO_4$

Material	$\alpha_V \cdot 10^{-6}$, 1/K
Zn_2SiO_4	8.05
$Zn_{1.9}Cu_{0.1}SiO_4$	8.81
Porcelain	5.5–7.0
Earthenware	7.0–8.1
Majolica	8.5–10.0

Colorimetric coordinates of blue-gray $Zn_{1.9}Cu_{0.1}SiO_4$ in the RGB color space consists of 71.8% red, 72.9% green and 79.6% blue (the percentages are relative to pure color), the color saturation is 16.1%.

Conclusion

The gray-blue pigment $Zn_{1.9}Cu_{0.1}SiO_4$ was obtained by the sol-gel synthesis method. The consequence of phase transformations during the synthesis of the $Zn_{1.9}Cu_{0.1}SiO_4$ solid solution was disclosed with the help of X-ray diffraction and thermal analysis. In situ high-temperature X-ray study for $Zn_{2-2x}Cu_{2x}SiO_4$ (x = 0; 0.05) in the range of 25–800 °C showed that the volume thermal expansion of the ceramic pigment reveals monotonic character. The calculated VTEC value for $Zn_{2-2x}Cu_{2x}SiO_4$ is close to VTEC reported for porcelain, earthenware, majolica.

Acknowledgements

The work was supported by UB RAS (project 18-10-3-32).

References

1. Berke H. The invention of blue and purple pigments in ancient times. *Chem. Soc. Rev.* 2007;36:15–30. DOI: 10.1039/B606268G.

2. Pozza G., Ajo` D., Chiari G., De Zuane F., Favaro M. Photoluminescence of the inorganic pigments Egyptian blue, Han blue and Han purple. *J. Cultural Heritage.* 2000;1:393–8. DOI: 10.1016/S1296-2074(00)01095–5.
3. Sidorov V. I., Malayvskyi N. I., Pokid`ko B. V. Poluchenie nizkoosnovnikh silikatov nekotorikh perekhodnikh metallov metodom osadzenizya. *Vestnik MGSU.* 2007;1:163–6. Russian.
4. Khleborodova O. A. Tablica sootvetstviya keramicheskikh mass I bazovikh glazurei [Internet]. 2017. Russian. Available from: https://www.ceramistam.ru/blog/Keramicheskie_massy/tablitsa-sootvetstviya-keramicheskikh-mass-i-bazovykh-glazurey/.

Please note that all new submissions will be accepted in English only. Requirements for the manuscript preparation are available on the Journal's website and in the following template

Chimica Techno Acta manusctipt style guidelines (title)

A.N. Authorname[a], A.N. Authorname[b], A.N. Authorname[ab]
a Institution, address, city, country
b Institution, address, city, country
e-mail: corresponding_author@e-mail.com

Abstract

The abstract should be a single paragraph (up to 300 words) in plain text (that means — no formulae or references are permitted) that summarises the content of the article. It should set the main objectives and results of the work; giving the reader a clear idea of what has been achieved. An abstract should not be extremely short though — if yours is 1–2 sentences long, then you're not doing it right. Make sure that you use well-known, searchable terms and phrases.

Keywords: short; searchable; keywords (up to 10).

Introduction

An introduction should 'set the scene' of the work. It should clearly explain both the nature of the problem under investigation and its background. It should start off general and then focus in to the specific research question you are investigating. Ensure you include all relevant references.

Experimental (if appropiate)

Descriptions of the experiments should be provided in enough detail so that a skilled researcher is able to repeat them. Methods already published or experimental techniques already described elsewhere should be indicated by a reference. Only non-standard apparatus should be described in details; commercially available instruments are referred to by their stock numbers.

Results and discussion

This is undoubtedly the most important section of your article. It should consist of the logically ordered sequence of text, formulae, images and tables.

All formulae which appear in their own line should be numbered:

$$A = B + C \tag{1}$$

Tables should be used only when they can present information more efficiently than running text or even an image:

Table 1

Just an ordinary table without any sophisticated formatting applied

A	B	C	D
1	2	3	4
+	+	+	-

All illustrations should be of a high quality (300 dpi or higher) and should be placed in the flow of the text, not in the end of an article:

Fig. 1. Just an ordinary image

Please bear in mind that all illustrations and tables should fit smoothly within either single column (approx. 6 cm) or double column (approx. 12 cm) width.

Conclusions

Your conclusions should summarize the main paper, underline the interpretation of the key results and highlight the novelty and significance of the work. They may address some plans for relevant future work as well.

Acknowledgements (if appropiate)

All sources of funding such as grants should be declared here. Individuals who contributed to the research but are not co-authors may also be briefly acknowledged.

References

A reference should be indicated in square brackets in line with the text (e.g. [1]). The actual references in the reference list should be numbered in the order in which they appear in the text. In Chimica Techno Acta so-called Vancouver Citation Style is adopted almost as it is described in the following public domain textbook [1]:

1. Patrias K. Citing medicine: the NLM style guide for authors, editors, and publishers [Internet]. 2nd ed. Wendling DL, technical editor. Bethesda (MD): National Library of Medicine (US); 2007- [updated 2015 Oct 2; cited 2017 Jun 07]. Available from: http://www.nlm.nih.gov/citingmedicine

Note that opposed to [1] we omit the date of publication (leaving year only) of the referenced journal article, as almost all journals are continuously paginated throughout the volume. And another one — DOI or a hyperlink should always come last in a reference. These are the only major differences between our style and such described in [1], so when in doubt — you can always refer to [1], it contains tremendous number of well-organized examples.

For your convenience, below are some references to the different types of publications:

Books

2. Livingstone S. The Chemistry of Ruthenium, Rhodium, Palladium, Osmium, Iridium and Platinum. Oxford: Pergamon; 1973. 222 p.

3. Bard AJ, Faulkner LR. Electrochemical Methods: Fundamentals and Applications. 2nd ed. New York: John Wiley & Sons; 2001. 833 p.

Books not in English

4. Evdokimov AA, Efremov VA, Trunov VK, Kleyman IA, Tananaev IV. Soedineniya redkozemel'nykh elementov. Molibdaty, vol'framaty [Rare-earth elements' compounds. Molibdates, wolframates]. Moscow: Nauka; 1991. 267 p. Russian.

* Translation of the title in square brackets is not required, but highly desirable.

* For Cyrillic languages, such as Russian, please use consistent transliteration system. There are plenty, but we strongly recommend BGN/PCGN Romanization as it's one of the

easiest to read and implement (https://en.wikipedia.org/wiki/BGN/PCGN_romanization_of_Russian).

Journal articles

5. Zuev AYu, Tsvetkov DS. Oxygen nonstoichiometry, defect structure and defect-induced expansion of undoped perovskite $LaMnO_{3\pm\delta}$. Solid State Ionics. 2010;81(11–12):557–63. DOI:10.1016/j.ssi.2010.02.024

6. Shannon RD. Revised effective ionic radii and systematic studies of interatomic distances in halides and chalcogenides. Acta Cryst. 1976;A32:751–67. DOI:10.1107/S0567739476001551

7. Allred AL, Rochow EG. A scale of electronegativity based on electrostatic force. J Inorg Nucl Chem. 1958;5(4):264–8. DOI:10.1016/0022-1902(58)80003-2

* For the majority of chemical journals corresponding abbreviation is defined in Chemical Abstracts Service Source Index (CASSI, http://cassi.cas.org). If an abbreviation is not available there, please use the full name of a journal.

* Note that DOI of an article, when available, should always be provided.

Journal articles on the Internet (e.g. for online-only journals without DOI)

8. Tkach V, Nechyporuk V, Yagodynets P. Descripción matemática de la síntesis electroquímica de polímeros conductores en la presencia de surfactants. Avances en Química [Internet]. 2013[cited 2016];8(1):9–15. Spanish. Available from: http://erevistas.saber.ula.ve/index.php/avancesenquimica/article/download/6357/6168

Conference abstracts

9. Zuev AYu, Sereda VV, Malyshkin DA, Ivanov IL, Tsvetkov DS. Mechano-chemical coupling in double perovskites as energy related materials. In: Abstracts of the XX Mendeleev Congress on general and applied chemistry, Vol. 3; 2016 Sep 26–30; Ekaterinburg, Russia. p. 325.

10. Steparuk AS, Usachev SA, Tsvetkov DS, Sosnovskikh VYa, Zuev AYu. Novyy katodnyy material na osnove mayenita dlya elektrokhimicheskogo karboksilirovaniya organicheskikh soedineniy [New mayenite-based cathode material for electrochemical carboxylation of organic compounds]. In: Tezisy dokladov XXVI Rossiyskoy molodezhnoy nauchnoy konferentsii "Problemy teoreticheskoy i eksperimental'noy khimii" [Abstracts of XXVI Russian scientific conference for young scientists "Problems of theoretical and experimental chemistry"]; 2016 Apr 27–29; Ekaterinburg, Russia. p. 285–286. Russian.

Dissertations

11. ten Donkelaar SFP. Development of Stable Oxygen Transport Membranes [dissertation]. Enschede (The Netherlands): University of Twente; 2015. 140 p.

Patents

12. Chemezov OV, Batukhtin VP, Apisarov AP, Isakov AV, Zaikov YuP, inventors; Institute of High-Temperature Electrochemistry UB RAS, assignee. Sposob polucheniya nano- i mikrovolokon kremniya elektrolizom dioksida kremniya iz rasplavov soley. Russian Federation patent RU 2427526. 2011 Aug 27. Russian.

13. Menta E, Da Re G, Grugni M., authors; Cti Europe S.R.L., assignee. Derivatives of chromen-2-one as inhibitors of vegf production in mammalian cells. United States patent US20060122387 A1. 2006 Jun 8.

Chimica Techno Acta

Учредитель — Уральский федеральный университет имени первого Президента России Б. Н. Ельцина
620002, Россия, Екатеринбург, ул. Мира, 19

Редактор *Е. Е. Крамаревская*
Художник-оформитель *Е. Р. Даурова*
Верстальщик *В. К. Матвеев*

Свидетельство о регистрации
ПИ № ФС77-56172 от 15.11.2013

Адрес журнала:
Россия, 620000,
Екатеринбург, ул. Мира, 28, оф. Х-268
E-mail: t.a.pospelova@urfu.ru
Формат 70×100/16. Заказ № 321.
Тираж 500 экз.
Отпечатано в типографии
Издательско-полиграфического центра УрФУ
620000, Екатеринбург, ул. Тургенева, 4
Тел.: +7 (343) 350-56-64, 350-90-13
Факс: +7 (343) 358-93-06
E-mail: press-urfu@mail.ru

Founded by Ural Federal University named after
the first President of Russia B. N. Yeltsin
19, Mira St., Ekaterinburg, 620002, Russia

Journal Registration Certificate
PI № FS 77-56172 as of 15.11.2013

Principal Contact
Office X-268, Mira Str.,
620000, Ekaterinburg, Russia
E-mail: t.a.pospelova@urfu.ru

Format 70×100/16.
Circulation 500 cop.

Publisher — Ural Federal University
Publishing Centre
4, Turgenev St., 620000 Ekaterinburg, Russia
Phone: +7 343 350 56 64, +7 343 350 90 13
Fax: +7 343 358 93 06
E-mail: press-urfu@mail.ru